AFRL-RB-WP-TR-2009-3048

STOCHASTIC LOAD TRANSFER MODEL FOR FASTENED JOINTS

Adam K. Parks and Jorge Abanto-Bueno

Structural Mechanics Branch
Structures Division

FEBRUARY 2009
Final Report

STINFO COPY

AIR FORCE RESEARCH LABORATORY
AIR VEHICLES DIRECTORATE
WRIGHT-PATTERSON AIR FORCE BASE, OH 45433-7542
AIR FORCE MATERIEL COMMAND
UNITED STATES AIR FORCE

NOTICE AND SIGNATURE PAGE

This report was cleared for public release by the USAF 88th Air Base Wing (88 ABW) Public Affairs Office (PAO) and is available to the general public, including foreign nationals. Copies may be obtained from the Defense Technical Information Center (DTIC) (http://www.dtic.mil).

AFRL-RB-WP-TR-2009-3048 HAS BEEN REVIEWED AND IS APPROVED FOR PUBLICATION IN ACCORDANCE WITH ASSIGNED DISTRIBUTION STATEMENT.

*//signature//   //signature//

_____   _____
ADAM K. PARKS   ANDREW G. SPARKS, Chief
Project Engineer   Structural Mechanics Branch
Structural Mechanics Branch   Structures Division
Structures Division

//signature//

_____
WILLIAM G. BARON
Technical Advisor
Air Vehicles Directorate

This report is published in the interest of scientific and technical information exchange, and its publication does not constitute the Government's approval or disapproval of its ideas or findings.

*Disseminated copies will show "//signature//" stamped or typed above the signature blocks.

REPORT DOCUMENTATION PAGE

The public reporting burden for this collection of information is estimated to average 1 hour per response, including the time for reviewing instructions, searching existing data sources, searching existing data sources, gathering and maintaining the data needed, and completing and reviewing the collection of information. Send comments regarding this burden estimate or any other aspect of this collection of information, including suggestions for reducing this burden, to Department of Defense, Washington Headquarters Services, Directorate for Information Operations and Reports (0704-0188), 1215 Jefferson Davis Highway, Suite 1204, Arlington, VA 22202-4302. Respondents should be aware that notwithstanding any other provision of law, no person shall be subject to any penalty for failing to comply with a collection of information if it does not display a currently valid OMB control number. **PLEASE DO NOT RETURN YOUR FORM TO THE ABOVE ADDRESS.**

1. REPORT DATE *(DD-MM-YY)*	2. REPORT TYPE	3. DATES COVERED *(From - To)*
February 2009	Final	26 February 2003 – 23 November 2008

4. TITLE AND SUBTITLE STOCHASTIC LOAD TRANSFER MODEL FOR FASTENED JOINTS	5a. CONTRACT NUMBER In-house
	5b. GRANT NUMBER
	5c. PROGRAM ELEMENT NUMBER 0602201
6. AUTHOR(S) Adam K. Parks (AFRL/RBSM) Jorge Abanto-Bueno (Bradley University)	5d. PROJECT NUMBER A02P
	5e. TASK NUMBER
	5f. WORK UNIT NUMBER 0C

7. PERFORMING ORGANIZATION NAME(S) AND ADDRESS(ES)		8. PERFORMING ORGANIZATION REPORT NUMBER
Structural Mechanics Branch (AFRL/RBSM) Structures Division Air Force Research Laboratory, Air Vehicles Directorate Wright-Patterson Air Force Base, OH 45433-7542 Air Force Materiel Command, United States Air Force	Bradley University Peoria, IL 61625	

9. SPONSORING/MONITORING AGENCY NAME(S) AND ADDRESS(ES)	10. SPONSORING/MONITORING AGENCY ACRONYM(S)
Air Force Research Laboratory Air Vehicles Directorate Wright-Patterson Air Force Base, OH 45433-7542 Air Force Materiel Command United States Air Force	AFRL/RBSM
	11. SPONSORING/MONITORING AGENCY REPORT NUMBER(S) AFRL-RB-WP-TR-2009-3048

12. DISTRIBUTION/AVAILABILITY STATEMENT
Approved for Public Release; distribution unlimited.

13. SUPPLEMENTARY NOTES
PAO Case Numbers: 88ABW-2009-0866; clearance date 04 March 2009. Report contains color.

14. ABSTRACT
In the investigation presented in this document, the capabilities and limitations of two well-know full-field techniques, namely the digital image correlation (DIC) and the thermoelastic stress analysis (TSA), are assessed. The main goals of this project are to assess the limitations of the two experimental techniques, determine if either technique can detect differences in the strain field of varying clamping loads, and subsequently compare the experimental results to a finite element model (FEM). Double-lap shear joint specimens made of aluminum 2024 and having three clamping torques were tested using both techniques. All the specimens were subjected to eight low-frequency varying-amplitude-loading. The DIC measurements provided the distribution of the in-plane displacement over the joint. The in-plane strain distribution over the same area was calculated from the measured displacements by applying least-squares minimization. The assessment of the in-plane strain distribution allowed identification of the location of regions subjected high levels of normal and shear strains around the joint. The analysis of the FEM model agreed to within 8 percent of the DIC measurements when the friction coefficients between the different surfaces in contact were reduced to 25 percent of their published values. *Continued on back*→

15. SUBJECT TERMS
Digital Image Correlation; Thermoelastic Stress Analysis; full field; lap joint; strain measurement technique; displacement measurement technique

16. SECURITY CLASSIFICATION OF:			17. LIMITATION OF ABSTRACT:	18. NUMBER OF PAGES	19a. NAME OF RESPONSIBLE PERSON (Monitor)
a. REPORT Unclassified	b. ABSTRACT Unclassified	c. THIS PAGE Unclassified	SAR	74	2d Lt Adam K. Parks 19b. TELEPHONE NUMBER *(Include Area Code)* (937) 904-6937

14. ABSTRACT, concluded

As the Air Force continues to pursue aircraft designs that push the limits of data on materials and structures, it is important to develop full-field experimental techniques to measure the displacement, strain and/or stress distribution over a region of interest of a strained body. The main advantage of full-field techniques over point-wise methods such as the use of strain gages is that they can easily provide the information of the different regions under high levels of strain or stress by just carrying out a single experiment. In the investigation presented in this document, the capabilities and limitations of two well-know full-field techniques, namely the digital image correlation (DIC) and the thermoelastic stress analysis (TSA), are assessed. The main goals of this project are to assess the limitations of the two experimental techniques, determine if either technique can detect differences in the strain field of varying clamping loads, and subsequently compare the experimental results to a finite element model (FEM).

Double-lap shear joint specimens made of aluminum 2024 and having three clamping torques were tested using both techniques. All the specimens were subjected to eight low-frequency varying-amplitude-loading cycles under load control conditions at a rate of 50 lbf/s. In the case of the DIC technique the load was kept constant for fifteen seconds at the valley and peak of each cycle. While in the case of the TSA technique, constant- amplitude oscillating load (50 lbf) at a frequency of 8 Hz was applied at the peak and valley of each loading cycle. Two 1280- by 960-pixel charge-coupled device (CCD) cameras and a 320- by 256-pixel infrared (IR) camera were used in the DIC and TSA experiments, respectively. Images around the joint were captured by the two CCD cameras at rate of two frames per second throughout the entire DIC experiment. The IR camera recorded the change in temperature around the joint only at the peak and valley of each loading cycle.

The DIC measurements provided the distribution of the in-plane displacement over the joint. The in-plane strain distribution over the same area was calculated from the measured displacements by applying least-squares minimization. The assessment of the in-plane strain distribution allowed identification of the location of regions subjected high levels of normal and shear strains around the joint. The analysis of the FEM model agreed to within 8 percent of the DIC measurements when the friction coefficients between the different surfaces in contact were reduced to 25 percent of their published values. The TSA measurements provided minimal information about the mechanical response of the joint, since the change in temperature measured by this technique was the same for all the peak and valleys. This was due to the way the cycling loading was applied.

TABLE OF CONTENTS

Section   **Page**

LIST OF FIGURES

LIST OF TABLES

1.0 INTRODUCTION

The Air Force faces many challenges while trying to maintain its technological superiority in the world. One of these challenges is two-fold: develop a methodology to create accurate models of aircraft structures that could be subjected to different loading conditions while reducing the number of experiments needed to validate such models. After accounting for new materials, new fabrication techniques, and extreme environments, full scale testing is financially unobtainable. Thus, engineers are forced to solve problems with unvalidated, questionable accuracy models. For example, one of the most prevalent structures on an aircraft is the bolted joint. However, this joint is often oversimplified in finite element models. This increases the model uncertainty and can produce unreliable results. Therefore, more accurate models are necessary to predict the early damage of joints as well as accurately predicting the fracture response of the strained structures. In order to overcome this drawback, new full-field experimental techniques must be tested and fully validated. By using the accurate full-field techniques, engineers can capture the physics occurring during testing and apply that knowledge to subsequent models. For this reason, the Structural Mechanics branch of the Air Vehicles Directorate conducted an in-house research project to measure the strain fields around mechanically fastened double-lap shear joint specimens using two new full-field experimental techniques: digital image correlation (DIC) and thermoelastic stress analysis (TSA). Using these measurements, a model to predict the failure of this type of joint was created.

This report documents the design, testing, and analysis of the Stochastic Load Transfer Model for Fastened Joints project. The main goal of this investigation is to enhance the knowledge available concerning the fracture behavior of mechanically fastened joints by measuring, using the digital image correlation technique and thermoelastic stress analysis, the whole deformation process around a fastener having different clamping torques and subjected to different loading/unloading conditions. To accomplish this objective, the project gathered data from a series of experiments using DIC and TSA. Following the experiments, a finite element model of the joint was created to attempt to reproduce the experimental results. Comparisons were then made between the experimental techniques and the finite element (FE) model. The key performance parameter thresholds for the project were a computer model accurate to within 70% of the stress near the hole, and a comparison between the DIC and TSA results with accuracy within +/-500psi.

This document has been divided into five main sections: introduction, experimental procedure, finite element model, results and discussion, and conclusions and recomendations. The next section deals with the experimental procedure where the specimen material, dimensions and preparation are described in detail. The specific experimental set-up required by each technique and the loading conditions applied during the experiments are also presented in this section. The procedure used to model the experiments is outlined in the finite element analysis section. The experimental and numerical results are presented next, and in the last section, conclusions and recommendations are given.

2.0 EXPERIMENTAL PROCEDURE

2.1 Test Articles

In order to maintain relevancy to the Air Force, the test articles were developed incorporating common aircraft materials and structure. The double-lap shear joint was chosen as the representative structure because its design should minimize any bending moment during testing. Any bending during the testing would negatively impact the results of the experiments. Aluminum alloy 2024-T3 was chosen because it is a commonly used material on aircraft.

The specimen consisted of two $9.00in$–long central plates and two $7.00in$–long doublers. The cross section of a typical central plate and doubler was $3.00in \times 0.19in$ and $2.00in \times 0.064in$, respectively. A $0.19in$ diameter hole was drilled at one inch from each edge of the doubler and at $2.50in$ from one end of the central plate resulting in a doubler width-to-hole-diameter (*w/d*) ratio of 10.53 and an edge-distance-to-hole-diameter (*e/d*) ratio of 5.26. The frontal and top orthographic views of the specimen are shown in Figure 1. The central plates and the doublers were connected with No. 10 NAS 6303 fasteners. A No. 10 steel, zinc plated washer was placed under the head of each bolt. NAS 1726 self-locking nuts were also used to assemble the specimen.
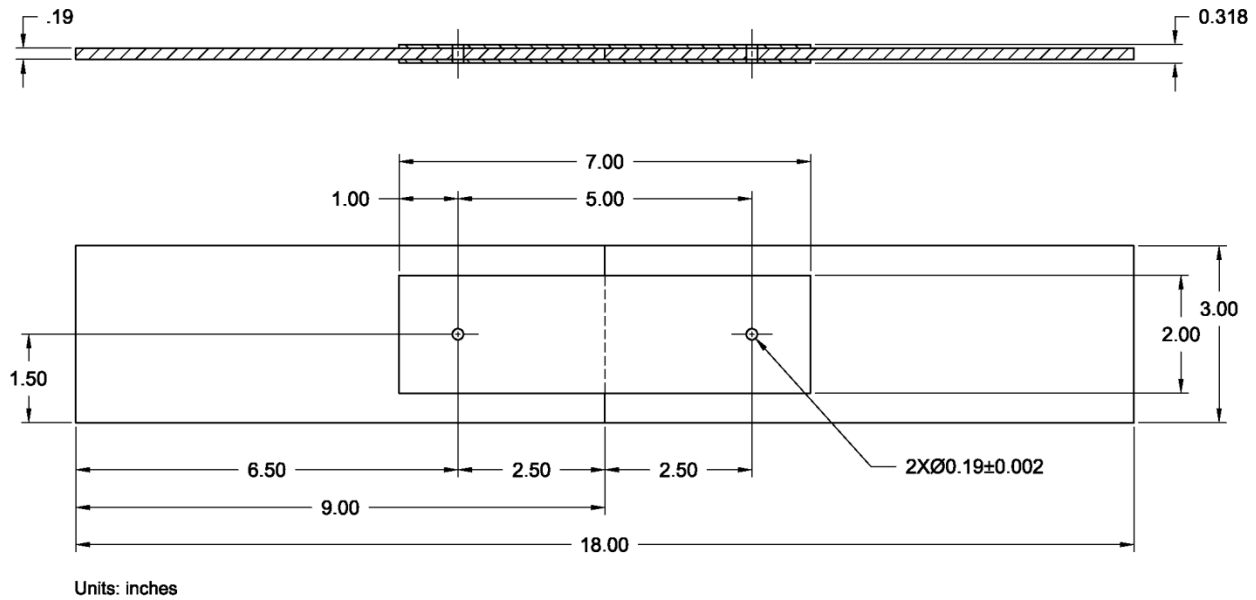
Figure 1: Dimensions of a typical double-lap shear joint specimen

In order to have accurate stress-strain curves for both the central plates and the doublers, information that is necessary to model the specimen in Abaqus/CAE (see next section), a total of five ASTM E8-04 standard subsize tension specimens were cut from the same sheets used to make the central plates and doublers[1]. The uniaxial tension tests, the results of which are shown in Table 1, were carried out under displacement control conditions at a rate of $0.05\ in/min$.

Table 1: Mechanical properties of the double-lap shear joint specimen components

Specimen Component	0.02% Young's Modulus, (Msi)	Yield Strength, (ksi)	Ultimate Tensile Strength, (ksi)	Elongation at Break (%)
Doubler	9.50	50.30	70.00	22
Central plate	8.60	44.30	57.50	20

A total of 18 test articles were used in this investigation: half were tested using the DIC technique and the other half with the TSA. All the central plates and doublers were thoroughly cleaned to remove any oily substances adhered to their surfaces during the machining process. Once the components had dried, the test articles were assembled using a click-type torque wrench. Since one the objectives of this investigation was to study the effect of the clamping force on the mechanical response of the joint, each set of nine articles was broken into three groups of three and tightened using the following torques: $30\ in \cdot lb$, $50\ in \cdot lb$ and $70\ in \cdot lb$. The SAE Aerospace recommended tightening torque for the fastening system used in this investigation is $47\ in \cdot lb$ [2]. Therefore, the selected torques provided information about the response of the joint to under– and over–clamping conditions.

2.2 Experimental Set-up

As mentioned in the introduction section, two different full-field techniques were used in this investigation, namely DIC [3-5] and TSA [6,7]. The former directly measures the in–plane displacement and strain fields throughout the area of interest, and the latter measures the change in temperature in the region of interest, which is later related, in the post–processing phase, to the sum of the change of the in–plane principal stresses generated by the applied load. In order to accurately measure these physical fields, the surface of the specimens must be prepared accordingly. A brief description of the experimental set-up used with each technique is given below.

2.2.1 DIC

The DIC method is a robust technique used to accurately measure deformations (displacement and displacement gradient fields) in a region of a strained body by comparing the local features of a pair of digital images taken before and after deformation of the body under investigation. There are two main requirements to successfully apply this technique: (*i*) the light intensity distribution on the surface of the body must be uniform and constant during the entire deformation process and (*ii*) the deformation must be locally homogeneous. This technique requires a random speckle–pattern on the region of interest of the test article. This step is necessary to perform, during the post–processing phase, the correlation between the undeformed and deformed states (digital images) of the area of interest. In this investigation, the region of interest was a $2in$ diameter area centered at one of the fasteners on both sides of the specimen. The speckle–pattern was generated using a fine airbrush and black water-based paint resulting in small dots a few microns in diameter, as can be seen in Figure 2. The coordinate system used in the DIC measurements (see Results and Analysis section) are also shown in Figure 2. The images correspond to the undeformed state of each region of interest: the side of the self-locking

nut (Figure 2(a) and the corresponding opposite side to the bolt head (Figure 2(b)). The x and x'-axis run parallel to the loading direction, while the y and y'-axis are perpendicular to it.

During the experiments, images of the area of interest are taken at a rate of 2 frames per second during the entire 978 seconds that each test lasted. The images were captured by two high resolution (1280×960 pixels) digital CCD cameras (Sony Corporation, model XCD-SX910) at a rate of 2 frames per second (fps) during 978 seconds (the time that each experiment lasted). Fire-i^{TM} (Unibrain Inc.) software controlled the two CCD cameras and allowed images of both sides of a joint to be captured almost simultaneously. There was a delay of only $100\ ms$ between the images taken of either side of the joint. Figure 3 shows the DIC test set–up used in this investigation. As seen in this figure, each camera was mounted on a stand that allowed horizontal and vertical movement. Accurate positioning of each camera was achieved with a computer–controlled stepper motor for each axis of motion. Each camera was positioned such that the bolt head on one side and the self-locking nut on the opposite side were in the center of the region of interest (see Figure 2). Fluorescent lights were used to light each side of the specimen to ensure a uniform distribution of the light over the areas of interest (see Figure 3).

(a)   (b)
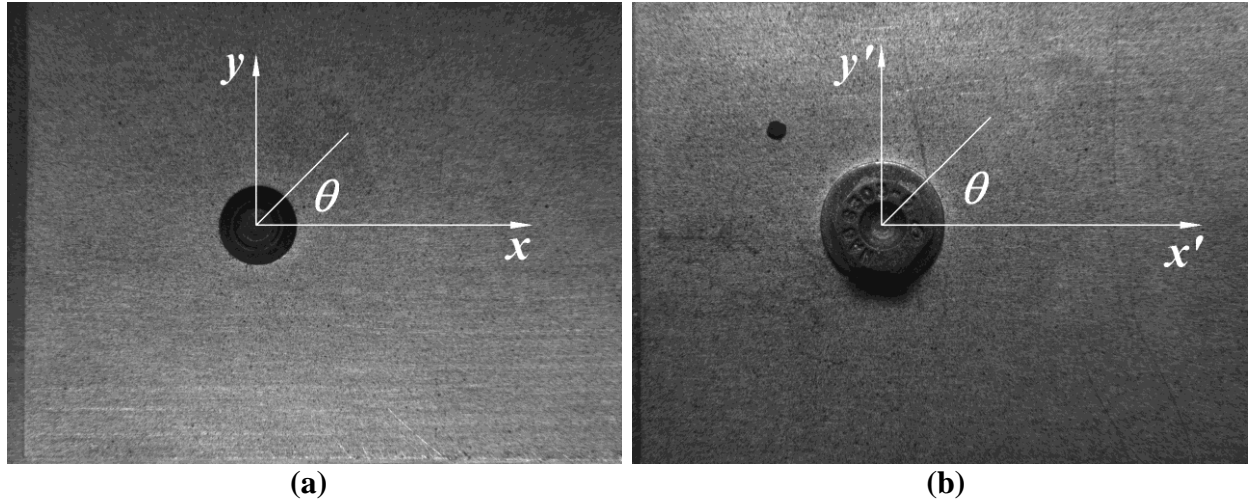
Figure 2: Typical random speckle-pattern of the region of interests of a double-lap shear joint specimen: (a) self-locking nut side and (b) bolt head side

The deformation (displacement and strain fields) is determined by postprocessing the images with an appropriate algorithm. In this investigation, a hybrid DIC scheme having three steps was used. This approach combined the two most accepted DIC minimization methods available in the literature, the Coarse-fine [3,4] and Newton–Raphson [5] methods. The three steps of the hybrid scheme are:

1. Determine an approximate displacement field with a variation of the Coarse-fine method ignoring any displacement gradients;
2. Determine an approximate strain field by numerically differentiating the approximate displacement field obtained in step 1;
3. Compute the actual displacement and strain fields using the Newton-Raphson approach with the approximate displacement and strain fields obtained in steps 1 and 2 as initial conditions.

With this approach, the computational time is considerably reduced over the traditional DIC Coarse-fine technique without losing accuracy, which is ensured by using the Newton-Raphson approach in the third step. This technique has been successfully used in mechanical characterization of advanced materials, quasi-static and dynamic fracture mechanics, and plastic deformation of materials [8-13].
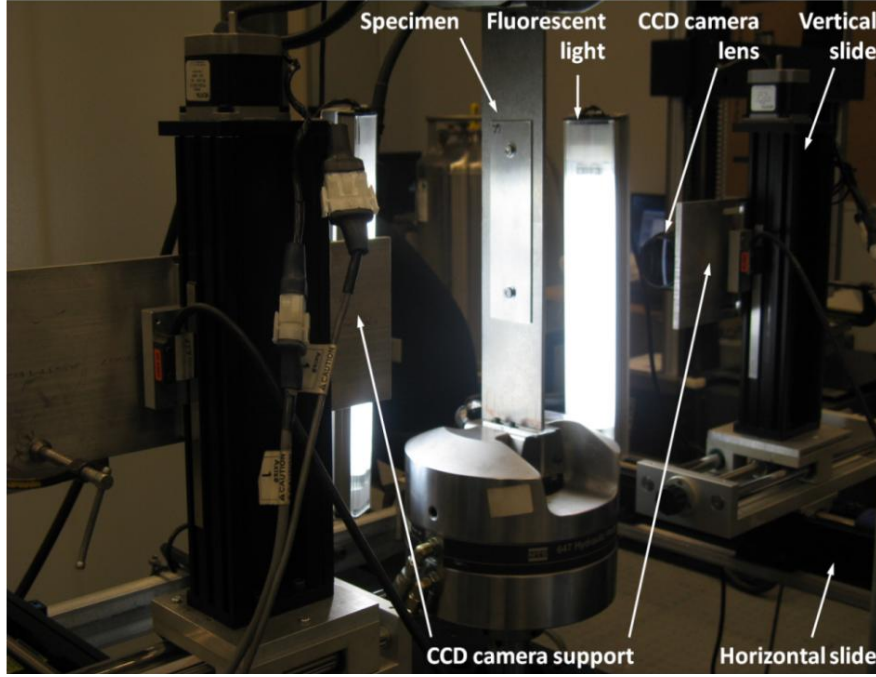
Figure 3: DIC experimental set-up

2.2.2 TSA

TSA is a full-field technique that is based on the fact that when a solid is loaded in compression or tension, the temperature of the body slightly increases or decreases (on the order of a few tenths of a degree), respectively. Therefore, when a solid is subjected to dynamic loading (in tension, compression, or both) the change in temperature ΔT of the surface of the body can be linearly related to the sum of the in-plane principal stresses range, $\Delta\sigma_1 + \Delta\sigma_2$, provided that (*i*) the total applied load does not exceed the elastic region of the body under investigation and (*ii*) the load is applied under adiabatic conditions (*i.e.*, there is no heat transfer between the body and the ambient surrounding the body). The relationship between the in-plane principal stress range and the change in temperature is given by the equation: [7]

$$\Delta\sigma_1 + \Delta\sigma_2 = -\frac{\rho C_P}{\alpha T}\Delta T \qquad (1)$$

where
ρ : Solid density
α : Coefficient of thermal expansion
C_P: Specific heat at a constant pressure
T : Ambient temperature

This technique uses a differential TSA system that includes a camera which has a focal plane array of InSb infrared (IR) detectors. Each detector measures IR radiation at a specific point on the surface of the body under investigation. In addition, the system has high-speed digital processing electronics to convert, at frame rates of up to 1000 frames/second, the measured radiation photon flux to change in temperature and thus the in-plane stresses range (see Eq. 1). The system requires (*i*) a temporally varying load such that the temperature changes are measured by time-averaging the dynamic load and (*ii*) a reference signal that must be proportional to the applied load such that the system can filter the IR background noise and extract the data corresponding to the applied load from the raw IR detector signal.

In this investigation the DeltaTherm system (Stress Photonics Inc.) was used, which has a camera (model DT1560) containing an array of 320×256 IR detectors. The DeltaTherm system records the thermal variations of the area of interest and generates an image showing the thermal changes using a color-based scale. Since the system collects radiation emitted from the surface of the strained body under investigation, the areas of interest on the double-lap shear specimens were fully coated with Krylon® flat black spray paint to reduce reflectivity and ensure high and uniform emissivity from the specimen surface. Figure 4 shows the self-locking nut side of the joint (area of interest) of a double-lap shear specimen having a coated area of approximately $2in \times 3in$ around the joint. A strain gage can be seen $2.5in$ to the left of the self-locking nut in Figure 4. Initially, the strain gage was to provide the reference signal needed by the DeltaTherm system to filter background noise. However, after a number of trials it was determined that the signal from the strain gage was too weak, and the signal provided by the load cell was used instead. Figure 5 shows the TSA experimental set-up. A black screen was placed behind the specimen to prevent the camera from capturing radiation from other objects.
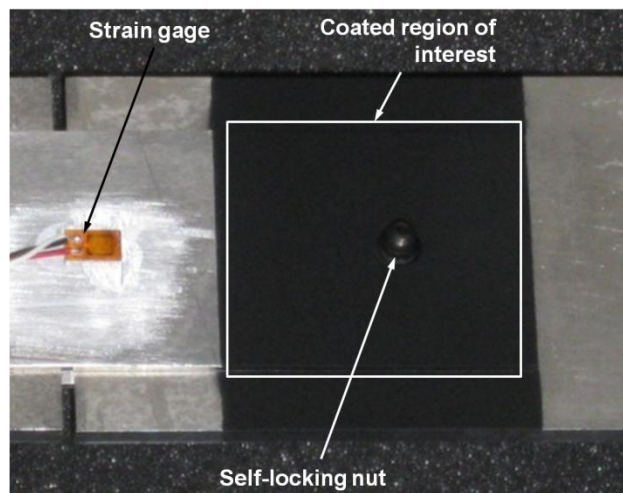
Figure 4: Double-lap joint specimen showing an area of approximately $3in \times 2in$ around the bolt head completely coated with flat black paint
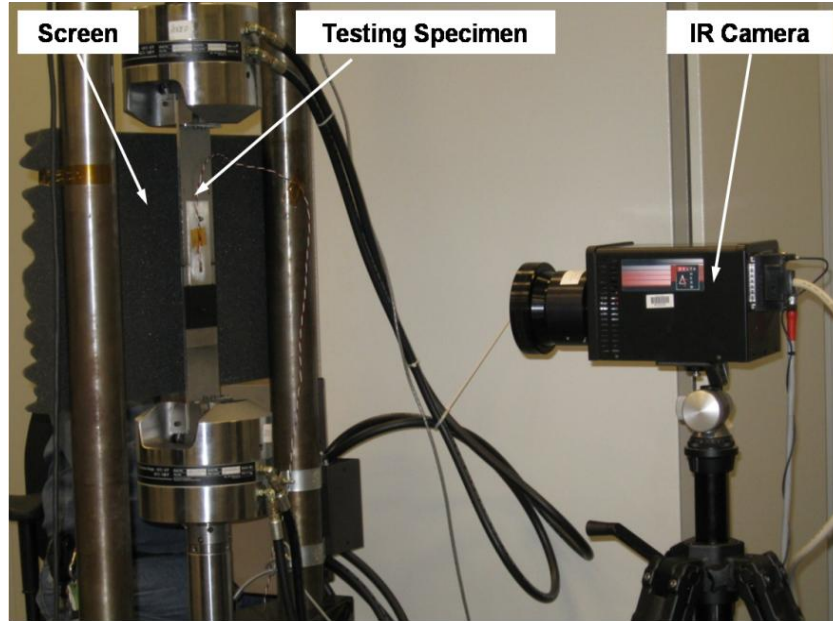
Figure 5: Thermoelastic stress analysis experimental set-up

2.3 Loading Conditions

All the tests were carried out using a standard closed-loop hydraulic uniaxial testing machine outfitted with three-inch wide MTS® hydraulic grips and a 20 kip load cell. Approximately $1.50 in$ from one extreme of each central plate was placed in the hydraulic grips to ensure uniformly distributed loading along the cross-section of the test article (see Figures 3 and 5). The testing machine was controlled using Multipurpose TestWare® Software (MTS Corporation), and the experiments were run under load control conditions at a rate of $50 lb/s$ following the loading profile shown in Figure 6. In the case of the DIC technique, each experiment lasted 978 seconds. As seen in this figure, the specimens were subjected to variable-amplitude cyclic loading with the loading ratio varying from 0.1 (50/500 1st cycle) to 0.01 (50/5000, 8th cycle). It can also be seen in Figure 6 that on every cycle the load was kept constant for 15 seconds at its valley ($50 lb$) and at its corresponding peak (*i.e.* $0.5\ kip, 0.85\ kip,$ $1.2\ kip, 1.7\ kip, 2.2\ kip, 3.2\ kip, 4.2\ kip, 5.0 kip$). This hold time was determined from a dummy experiment on an $18 in \times 3 in \times 0.19 in$ plate during which it was noted that the testing machine reaches its steady state at the valley and peak of each cycle after 5 seconds with an initial over/undershoot of +/-50 *lb* by the machine.

The loading profile was modified slightly for the TSA experiments to satisfy the requirements for a fluctuating load and adiabatic conditions. A sinusoidal load at a frequency of $8\ Hz$ and an amplitude of 50 *lb* was applied for 120 seconds at the valley and peak of each cycle, instead of a constant load for 15 seconds. The needed amplitude and frequency of the sinusoidal loading was determined during a dummy test. Measurements of the temperature change were carried out only during the valley and peak of each cycle and it corresponded to the average over 60 seconds after reaching steady state conditions (~ 30 seconds).
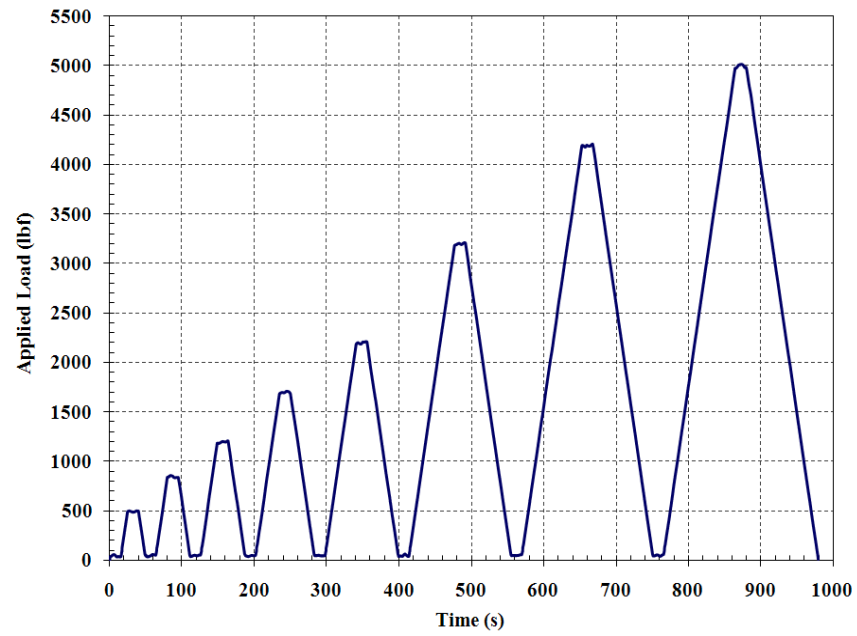
Figure 6: Typical loading profile used with the DIC technique

3.0 FEM

3.1 Building Block Approach to Model Verification

The construction and numerical analysis of the finite element model of the double-lap shear joint specimen was completed in ABAQUS/CAE 6.7–1[14]. In order to become familiar with the advanced techniques of this FEA software (e.g. modeling the contact between surfaces and clamping torque), a building-block approach was used to generate the complete model. The main phases of this approach are shown in Figure 7. Initially, the model consisted of only two plates held together with a pressure force. Subsequent models increased in complexity by adding holes, pins, and contact surfaces. Eventually, the model became a representative structure of the actual test article. The model was built to the same dimensions as the test article and included contact surfaces, holes, and headed pins to simulate the combination of the bolt/washers and bolt/self-locking nuts. The joint clamping torque was simulated using a bolt-load model, which will be described later in the section. The elastic-plastic response of the materials was entered into the analysis in the form of true stress-true strain that was determined from the data of the uniaxial tensile tests. Friction properties were initially taken from the literature and then modified to calibrate the model results to the experimental measurements. The following sections will describe in more detail how the final model was constructed.
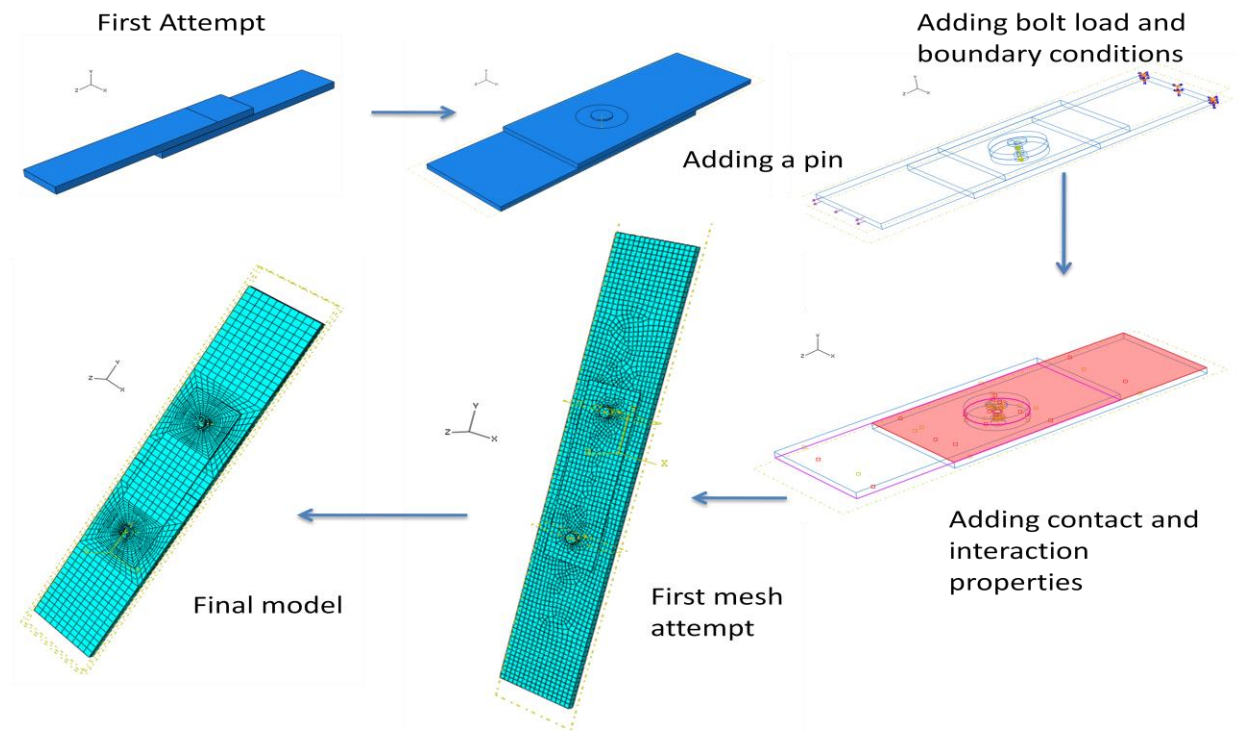
Figure 7: Building block approach to building the model

3.2 Model of Double-Lap Shear Joint Specimen

3.2.1 Pin as a representative structure

Many hours were spent to accurately and efficiently model the bolt connection in the model. At first, the bolt was modeled in its entirety, including its threads. The nut was fashioned in a similar manner. After some initial attempts to add contact between the threads and other contact surfaces, it was determined that the analytical benefits of including the threads did not outweigh the modeling obstacles of including the threads. The next attempt was at the other end of the spectrum, with a simple rod as the connecting device. It was quickly seen that by not including a bolt head or a nut, the fidelity sought in the model would not be achieved. Thus, the final representation of the bolt included a simple rod as the shaft of the bolt with the addition of a "nut" on the bottom and a "bolt head/washer" on the top of the shaft as shown in Figure 8. The "nut" was generated using a solid cylinder having a diameter and length equal to the major diameter and overall height of the self-locking nut, respectively. The "bolt head/washer" was constructed as a solid hexagonal prism fully attached to a thin disk using the dimensions of the head of the bolt and the washer, respectively. It is important to mention that no threads were modeled in this final representation. By using this simplified model, the bolted joint had the benefit of including the pressure forces due to both the head and the nut of the bolt, while remaining relatively simple in its geometry.
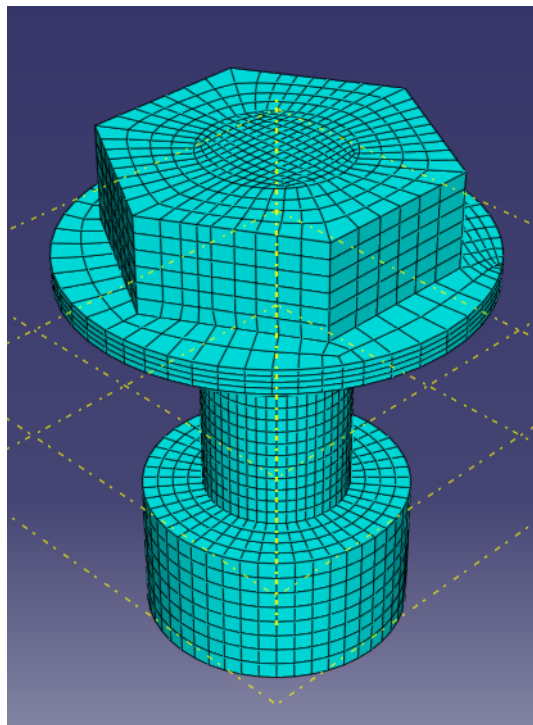
Figure 8: Model of a pin used as the representative structure of the aircraft bolt
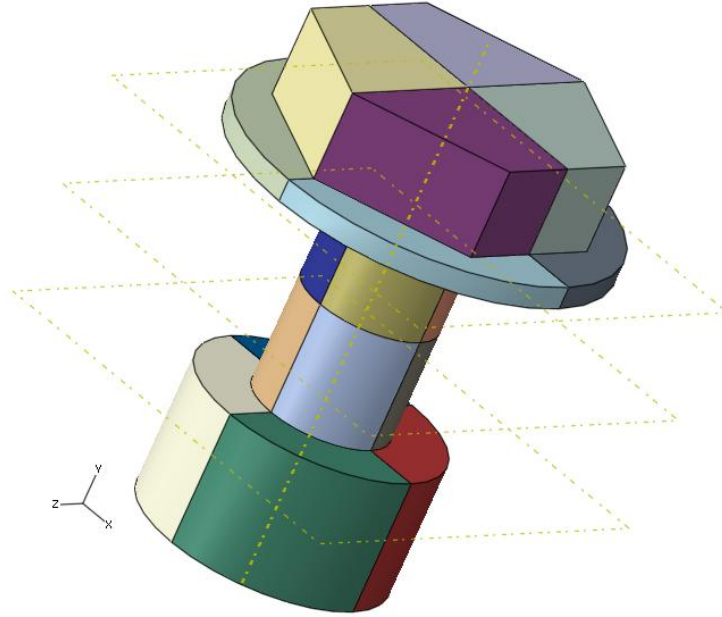
3.2.2 Model Partitions

The model of the double-lap shear joint included six parts: two central plates, two doublers, and two bolts. When all these parts were put together, a very complex model was generated, making

the meshing of the model a very taxing task. For example, regions that combined cylinders and prisms (e.g., around the joint) were the more difficult to mesh. Fortunately, one of the key characteristics of most FEA software, which aides the meshing of complex models, is the use of partitions, where complex geometries are split into simple ones. The main steps followed to mesh the model, based in part on the work of Iancu *et al.*[15], are outlined next. The doublers and central plates were partitioned, as seen in Figure 9, around each hole to facilitate meshing. Two to three concentric circles were drawn with increasing diameters increments of $0.75in$, respectively. A $2in$ square enclosed the concentric circles for the doubler while a $3in$ square was used for the central plates. To complete the partitioning, lines were drawn at 45° to the square corners to create an "X". Figure 9 shows each individual partition as a different color. By making these partitions, the structured meshing algorithm in ABAQUS could be used to mesh the rectangular regions, while the sweep meshing algorithm could be used for the regions surrounding the holes.
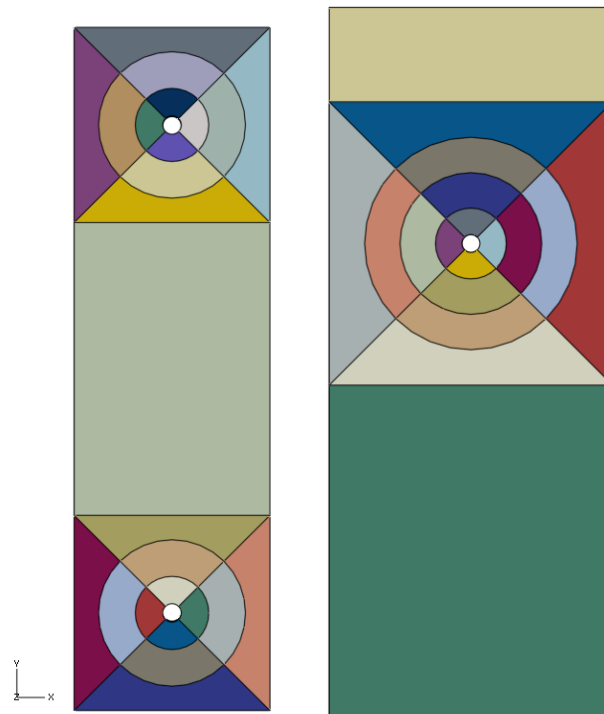
Figure 9: Doubler and Central plate Partitions

A similar approach was employed to partition the pins. The pins were quartered along the cylindrical shaft, and the shaft was divided in half. This separated the nut half from the head half of the pin. A partition was added at each end of the rod to separate the nut and bolt head from the shaft. Like Figure 9, Figure 10 shows each of the partitions as a different color. The structured meshing algorithm was used on the shaft, while the sweep meshing algorithm was used on the nut and bolt head regions.

**Figure 10: Pin partitions**

3.2.3 Mesh construction

After creating all the necessary partitions, the whole model was meshed starting around the bolt hole and progressing outward, partition by partition. Seven elements were used on each arc for the doublers, while eleven were used on each arc for the central plate. The difference in number of elements was to decrease mesh distortion occurring in the central plate mesh. The mesh of each pin contained twelve elements along the washer arcs; this was done to reduce mesh distortion in the hexagonal shaped top of the pin. Figure 11 depicts the final mesh on the test article. The mesh was generated using only C3D8R elements which are eight-node, reduced integration, linear bricks. These elements were chosen for three reasons: (*i*) they allowed the use of multiple meshing techniques like sweep and structure which constructed a better mesh; (*ii*) their reduced integration property reduced the computational cost compared to other elements; and (*iii*) since the model assembly has geometric and axial loading symmetry, there was no need to use elements that have rotational degrees-of-freedom. After the mesh was constructed, each doubler included 4256 elements, each central plate included 3920 elements, and each pin included 10424 elements.
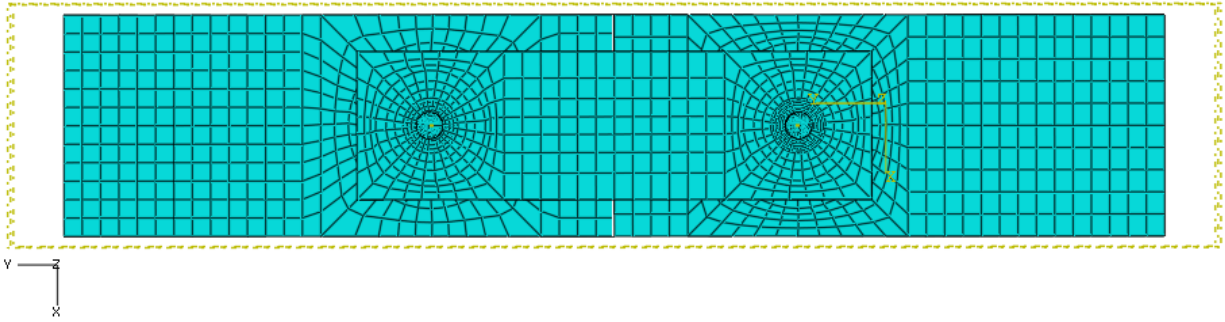
Figure 11: Mesh of full assembly

3.2.4 Bolt Load Model

In order to determine the best way of simulating the clamping torque on the joints, a series of simple simulations were ran and analyzed. First, a pressure was used to simulate the head of the bolt being pressed onto the surface of the doublers. The approach assumes that the clamping load is uniformly distributed over the entire area of the washer; an assumption that is incorrect.   Next, the bolt load model provided in ABAQUS was used. A key component of this model is the definition of a cross-sectional area along the length of the pin where the bolt load must be applied. To determine the best location, simulations were carried out applying the bolt load on three different surfaces along the length of the pin: (*i*) the surface at the middle of the pin, (*ii*) the surface at the intersection of the pin and the bolt head/washer, and (*iii*) the surface at the intersection of the pin and the nut. The planes where these surfaces are located are identified with arrows in Figure 12. From the analysis of the load distribution along the length of the pin, it was determined that the bolt load must be applied on the middle surface of the pin. Figure 12 shows the bolt load applied on the middle surface of our pin model.

13
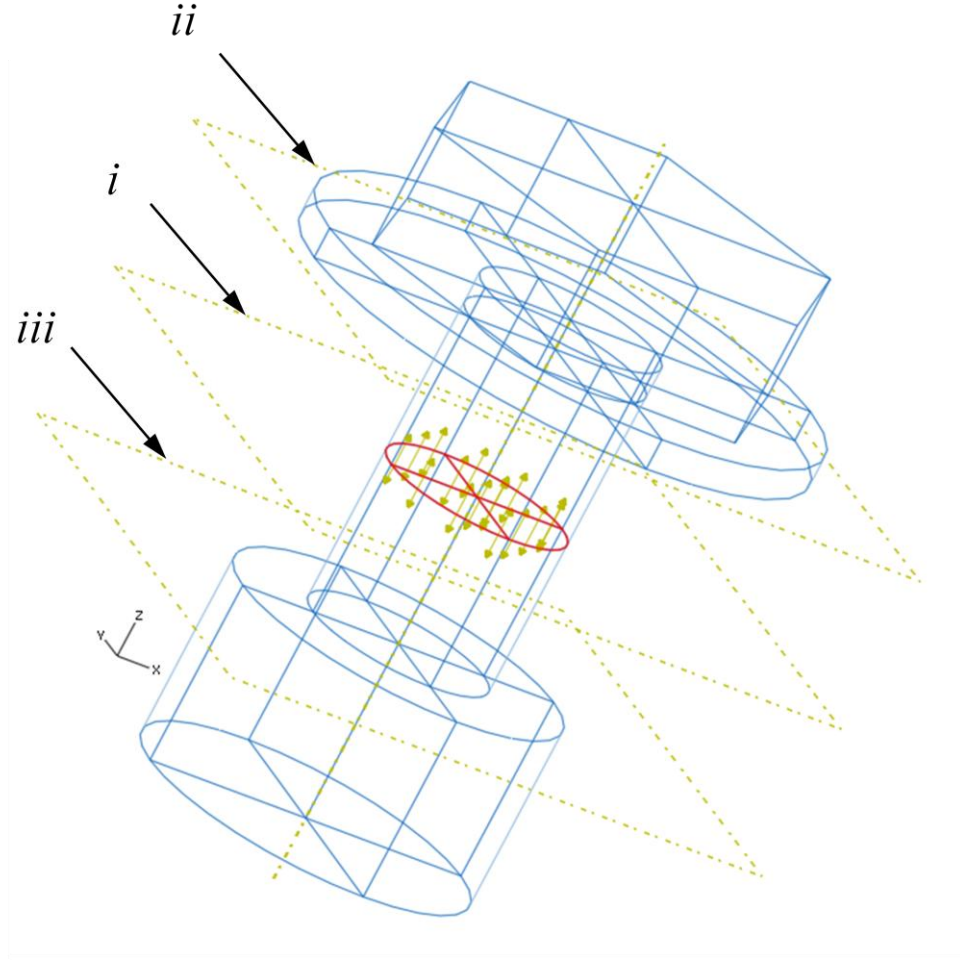
Figure 12: Bold load application

The magnitude of the bolt load that must be applied to the middle surface of the pin-bolt for the three torque conditions under investigation can be determined using the simplified torque formula

$$T = KF_id \qquad (2a)$$

where T is the applied torque, F_i is the unknown tension bolt load, d is the nominal major diameter of the bolt, and K is the correction factor that depends on the material size, surface friction, and threading of the bolt. K can be calculated from the formula[16]

$$K = \left(\frac{d_m}{2d}\right)\frac{\tan\psi + \mu\sec\alpha}{1 - \mu\tan\psi\sec\alpha} + 0.625\mu_c \qquad (2b)$$

where

d_m : thread mean diameter
ψ : thread helix angle

μ : friction coefficient between threads
α : thread angle
μ_C : friction coefficient between bolt head (or nut) and clamping surface

The commonly used value of K for dry mid-size steel bolts $K = 0.2$. Using this value, the known torques, and bolt diameter in Eq. (2a), the bolt load was determined for the three test conditions. The results are presented in Table 2.

Table 2: Calculated bolt load for each clamping torque condition

Applied Clamping Torque (in-lb)	Bold Load (lb)
30	793.65
50	1322.75
70	1851.85

3.2.5 Boundary and loading conditions

The reference frame used in the generation and analysis of the model is shown in Figure 13. As can be seen in this figure the load was applied in the negative *y*-direction. Two sets of boundary conditions were used to simulate the DIC experiment. The first set was applied to fully constrain the motion of the lateral surface of one of the central plates (shown on the left in Figure 13) simulating the action of the fixed grips of the testing machine on the testing article. This non-displacement condition remained the same throughout the whole simulation. The second set was placed on the lateral surface of the second central plate (right side on the model shown in Figures 13 and 14). In this case the boundary conditions were applied in two consecutive steps. First, during the application of the bolt load this surface was kept fixed (right side of the specimen in Figure13), and then immediately after the required bolt load was reached, the displacement condition was partially removed to allow only displacement in the *xy* plane (*i.e.*, no out-of-plane displacement) and at the same time surface traction was applied (right side of the specimen in Figure 14) following exactly the loading profile shown in Figure 6.
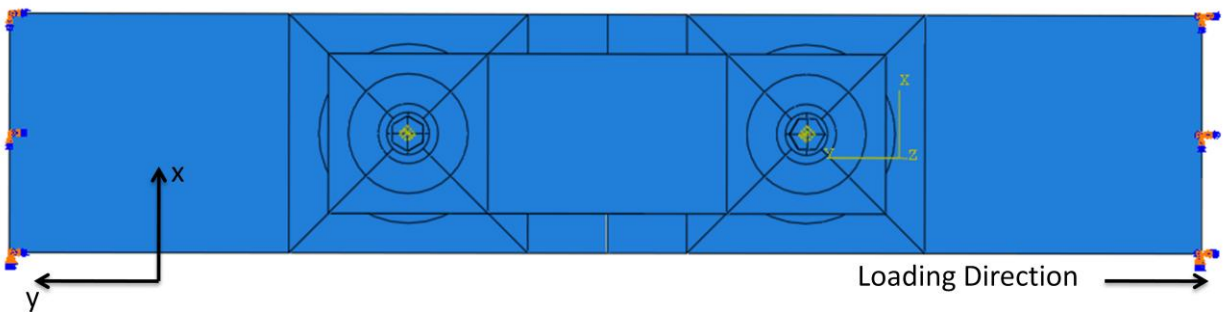
Figure 13: Model boundary conditions
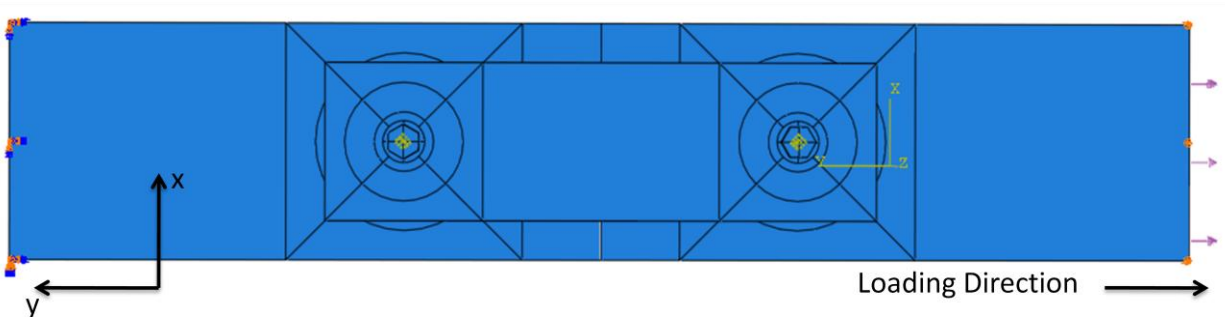
Figure 14: Location of the applied displacement and loading conditions

3.2.6 Surface contact and friction properties

To simulate the dry friction between the surfaces of the specimens, surface contact pairs were created, using the master-slave approach, between the doublers and the central plate (front and back), between the bore of the holes in the doublers and central plates and the pin shafts, between the pin heads and the doublers, and between the pin-nuts and the doublers. The surfaces of the pins were always the master because of they were more element dense around the holes than the other pieces. The central plates were always the master when paired with the doublers for the same reason. Figure 15 depicts the contact pairs used in the model. A moderate amount of sliding between components was expected; therefore, small sliding was selected for all interactions. From these contact pairs, interaction properties were defined for aluminum and aluminum, aluminum and stainless steel, and aluminum and zinc. These properties used the penalty method for friction formulation [14] and included both normal and tangential behavior.
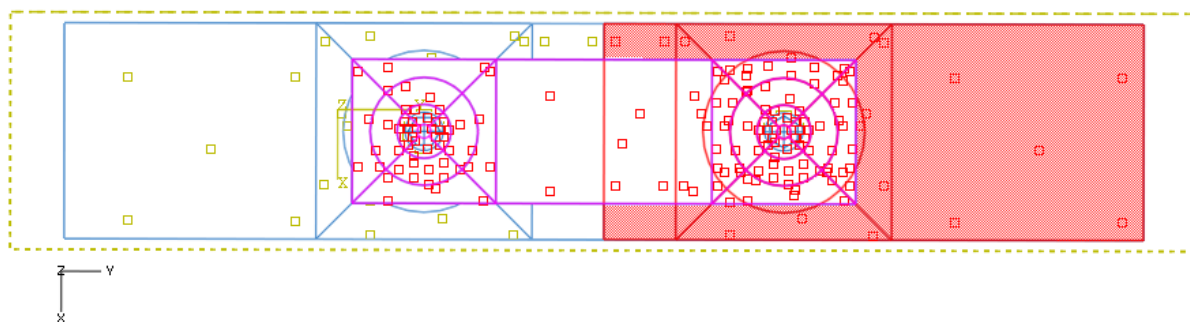
Figure 15: Example contact pair in model

3.2.7 Additional model properties

As previously mentioned, the uniaxial tensile test data was used to create the elastic-plastic material property models for the simulation. The doublers and the central plates each had different material properties based upon the tests conducted on each specimen. The results of these tests can be found in Appendix C, Figures C-1 and C-2. Additionally, due to the potential of plastic deformation, geometric nonlinearity was enabled for all steps in the simulation. Additional figures depicting the geometry, partitions, and mesh can be found in Appendix A.
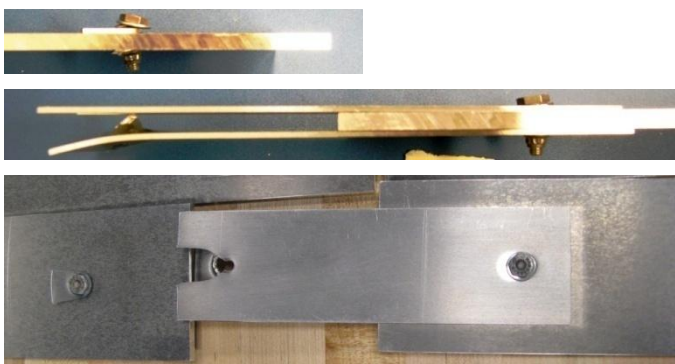
16

4.0 RESULTS AND DISCUSSION

4.1 Far-Field Measurements and Observations

4.1.1 DIC Experiments

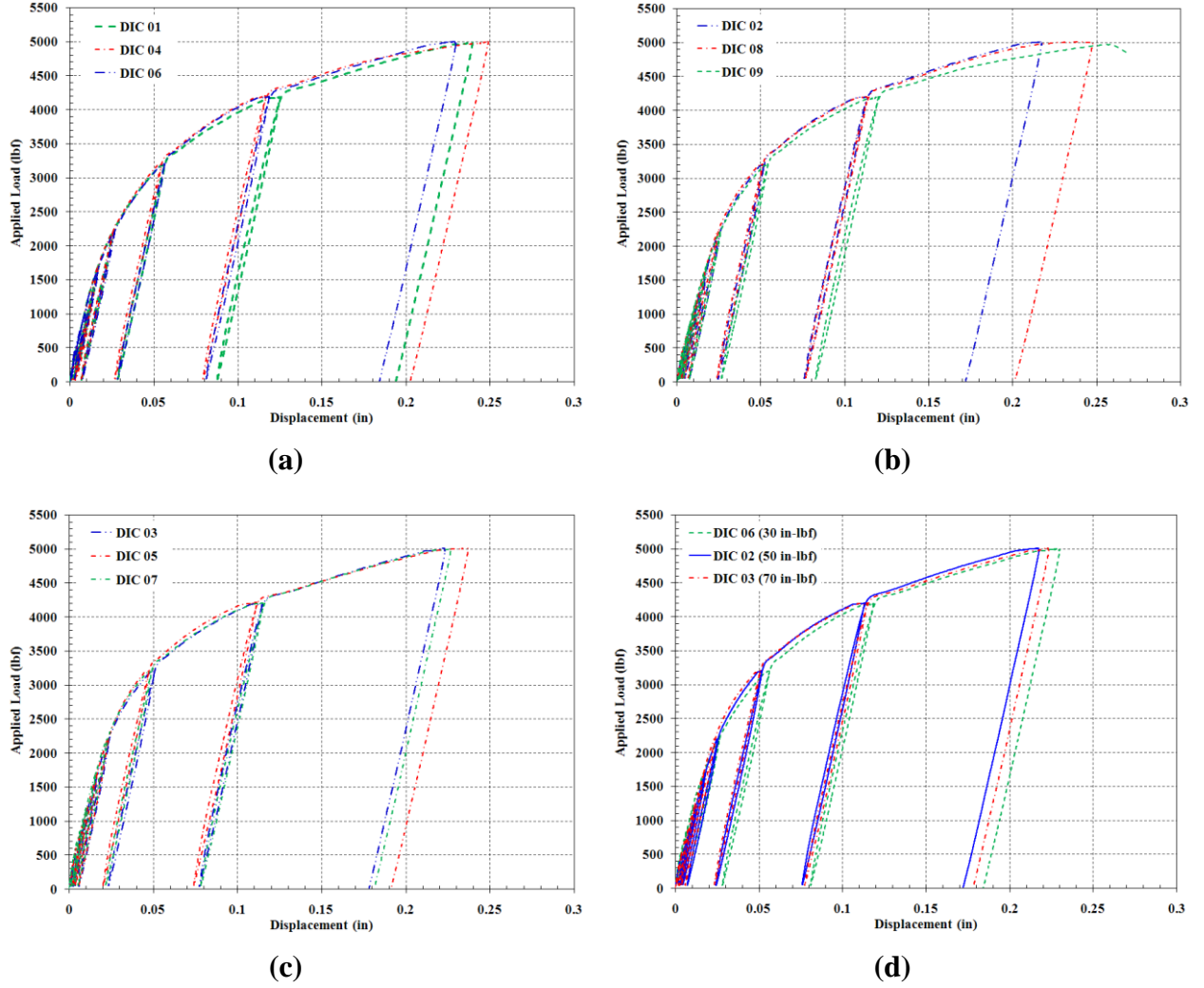Nine double-lap shear joint specimens arranged in three sets of three fastened clamping torques: $30\ in \cdot lb$ (undertorqued), $50\ in \cdot lb$ (recommended torque), and $70\ in \cdot lb$ (overtorqued), were tested following the loading profile shown in Figure 6. Careful examination of every specimen, carried out immediately after the test, revealed localized plastic deformation in the doublers but only around one of the joints. This permanent deformation was more pronounced in the region where the bearing load was transferred from the bolt to the doublers. Table 3 presents the name designation of each specimen used in the DIC experiments (name designation that will be used from now on in this document), the corresponding clamping torque, and the specimen post-mortem features. It can be noticed in Table 3 (third column) that in at least one of the specimens of each clamping set, namely specimens DIC 04 ($30\ in \cdot lb$), DIC 08 ($50\ in \cdot lb$) and DIC 05 ($70\ in \cdot lb$); one of the doublers bent. Unfortunately, this phenomenon did not always occur at the joint of interest where the CCD cameras were aimed (see fourth column of Table 3). It can also be seen that the doublers of specimens DIC 04 and DIC 08 exhibited similar bending that was more pronounced than the one displayed by the doubler of specimen DIC 05. As a result of the bending of the doubler, the bolt of the corresponding joint also showed extensive bending while slight bending was observed on the bolt at the other joint of the specimen. One of the doublers of specimen DIC 09, which was fastened using the recommended torque, failed completely by tearing, starting at the joint.

Table 3: DIC specimens: clamping torques, designation, and post-mortem features

Clamping torque ($in \cdot lb$)	Specimen Designation	Specimen Post-Mortem Features	Location of Doubler Bent
30	DIC 01		None
	DIC 04		DIC joint
	DIC 06		None
50	DIC 02		None
	DIC 08		Not DIC joint
	DIC 09		None
70	DIC 03		None
	DIC 05		Not DIC joint
	DIC 07		None

By comparing the post–mortem features of all the specimens (see Table 3) and especially of specimens DIC 04, DIC 05, DIC 08, and DIC 09, it can be inferred that the deformation/failure process of a double–lab shear joint specimen subjected to the loading profile shown in Figure 6 involves: (*i*) overcoming friction between surfaces in dry contact, (*ii*) continuously increasing localized plastic deformation around the joint caused by the bearing load, (*iii*) bending of both a doubler end and a bolt of one of the joints of the specimen caused probably by the increase of the cyclic load amplitude and (*iv*) failure of one of the joints by tearing out one of the doublers (specimen DIC 09). The far–field displacement response (cross–head displacement of the testing machine) of each specimen to the applied load (load cell measurement) for the conditions of undertorquing, recommended torque, and overtorquing is shown in Figures 16(a)–16(c), respectively. It can be seen in these figures that, during the first six loading cycles, all of the specimens having the same clamping condition presented very similar curve patterns, which can be related to the steps (i) and (ii) of the deformation process inferred from Table 3. With the increase of the loading amplitude in the last two cycles, one of the doublers and thus the corresponding joint bolt of specimens DIC 04 (30 $in \cdot lb$), DIC 08 (50 $in \cdot lb$), DIC 09 (50 $in \cdot lb$), and DIC 05 (70 $in \cdot lb$) underwent first bending and then failure as was the case of specimen DIC 09, which can be corroborated by the extensive displacement response exhibited by these specimens. Among the four specimens, specimen DIC 05 was the one that exhibited the smallest displacement response and thus lower bending of the doubler and joint bolt (See third column of Table 3).

(a)

(b)

(c)

(d)

Figure 16: Applied load versus displacement response of the double–lap shear joint specimens measured during the DIC experimemts for clamping torque of (a)$30 \ in \cdot lb$, (b) $50 \ in \cdot lb$, (c) $70 \ in \cdot lb$. The response of representative specimens for each clamping condition exhibiting only localized plastic deformation around the joint are shown in (d).

4.1.2 TSA Experiments

The applied load versus far-field displacement response of the double-lap shear specimens, for each clamping torque condition measured during the TSA experiments, is presented in Figure 17: (a) $30 \ in \cdot lb$, (b) $50 \ in \cdot lb$, and (c) $70 \ in \cdot lb$. It is important to remember that because of the adiabatic conditions required by the TSA technique (see Section 2.2.2) to measure the change of surface temperature of the body, the loading profile presented in Figure 6 was modified at the valley and peak of each cycle where sinusoidal loading at a frequency of $8 \ Hz$ and an amplitude of $50 \ lb$ was applied for 120 seconds. It can be seen that all the specimens failed before reaching the peak of the last loading cycle. All of the specimens fastened with a clamping torque of $50 \ in \cdot lb$ (recommended SAE torque) finished the 7th loading. However, only two specimens fastened with a clamping torque of $30 \ in \cdot lb$ and one fastened with a clamping torque of

$70\ in \cdot lb$ finished the 7th loading cycle. It seems that for a mechanically fastened joint subjected to the loading conditions similar to the ones used in these experiments, overtorquing will be more detrimental than undertorquing.

(a)

(b)

(c)
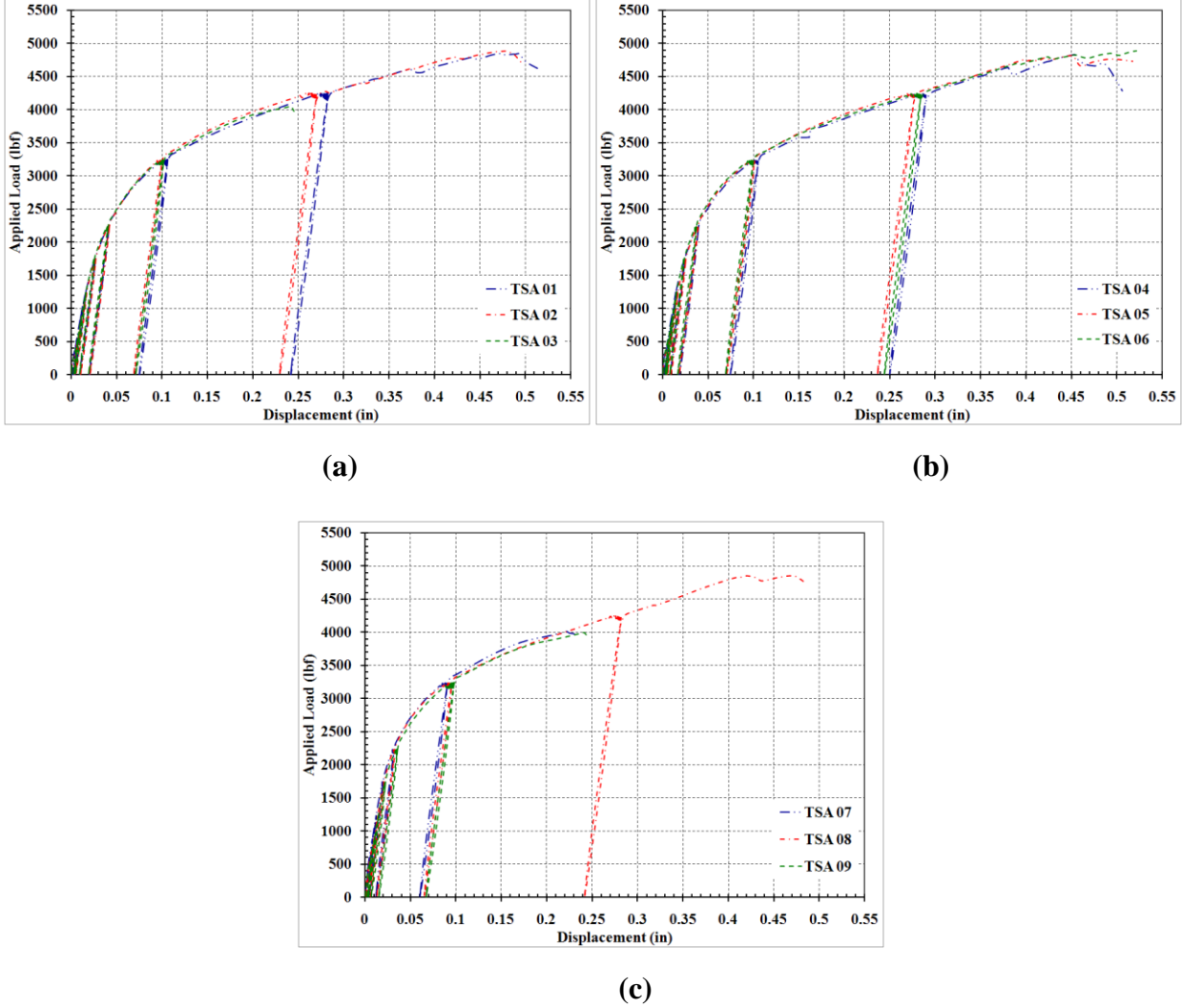
Figure 17: Applied load versus displacement from the TSA experiments for clamping torques of (a) $30\ in \cdot lb$, (b) $50\ in \cdot lb$, (c) $70\ in \cdot lb$

4.2 Near-Joint Deformation Field Measurements

4.2.1 DIC Measurements

The in-plane displacement and displacement gradients distribution around the joints of the specimens were measured using an in–house DIC algorithm previously validated and applied to different areas of solid and fracture mechanics [12,13]. The measurements are carried out by selecting a subset of pixels from the region of interest in the digital image of the undeformed specimen. This subset of pixels must possess a distinct grayscale pattern. This is ensured by generating a random speckled-pattern on the surface of interest of the testing article just before

the experiment (see Experimental Procedure section). The DIC algorithm searches for the selected subset of pixels on the digital image captured during the experiment (deformed state). Under the assumption that the subset of pixels is small enough such that it undergoes only homogeneous deformation, the difference between the deformed and undeformed digital images generates six parameters that completely defines the deformation of the pixel in the center of the subset: in–plane Cartesian displacement components u (x −direction) and v (y −direction), and displacement gradients $\frac{\partial u}{\partial x}, \frac{\partial v}{\partial y}, \frac{du}{dy}$, and $\frac{\partial v}{\partial x}$. By repeating the procedure described above using a large number of subsets (in the order of thousands), the distribution of the in–plane displacement components and displacement gradients can be measured throughout the region of interest. The distribution of the in–plane displacement components and the displacement gradients throughout the region of interest can be achieved by selecting a large number of subsets and repeating the comparison described above for each subset.

4.2.1.1 In-plane Displacement Fields

To illustrate the DIC measurements, Figure 18 shows images of both sides of one of the joints of specimen DIC 02 captured at the peak of the sixth cycle, $3.2 \, kip$ (Figures 18(a.1) and (b.1)), and the seventh cycle, $4.2 \, kip$ (Figures 18(a.2) and (b.2)). The corresponding *undeformed–state* images were presented in Figure 2. The deformation endured by the joint can easily be perceived from these images. The images in Figure 18 in combination with the ones of Figure 2 were used in the DIC algorithm to measure the in-plane displacement distribution. The results are shown in Figures 19 and 20 in the form of contour plots. Figure 19 shows contour plots of the displacement distribution along the x −direction (a) and y −direction (b) on the self-locking nut side of the joint for the two load levels defined in Figure 18: $3.2 \, kip$ ((a.1) and (b.1)) and $4.2 \, kip$ ((a.2) and (b.2)). In the same fashion, contour plots of the in–plane displacement distribution on the bolt head side of the joint are presented in Figure 20. The coordinate system used in the DIC measurements has its origin at the center of the bolt and the x–direction is parallel to the direction of the applied load as shown in Figure 2. It should be realized that, because of the location of the CCD cameras, the relationship between the axes of the coordinate systems used in the measurements at both sides of the joint are: $x = x'$ and $y = -y'$ (see Figure 2). The size of the subset used in the correlation was 35×35 pixels that corresponds to a physical area of $1.8mm \times 1.8mm$ and 8000 subsets were correlated with each pair of images.
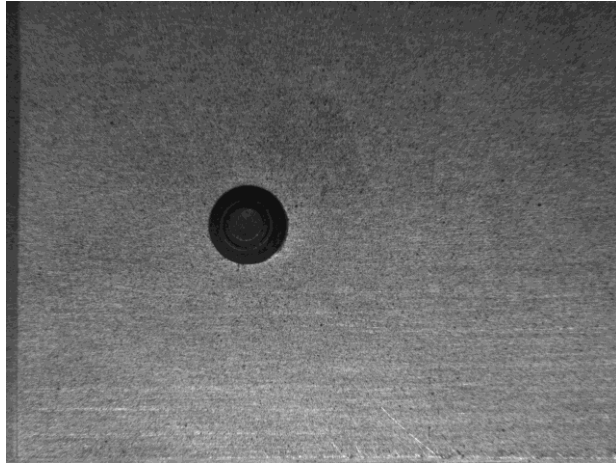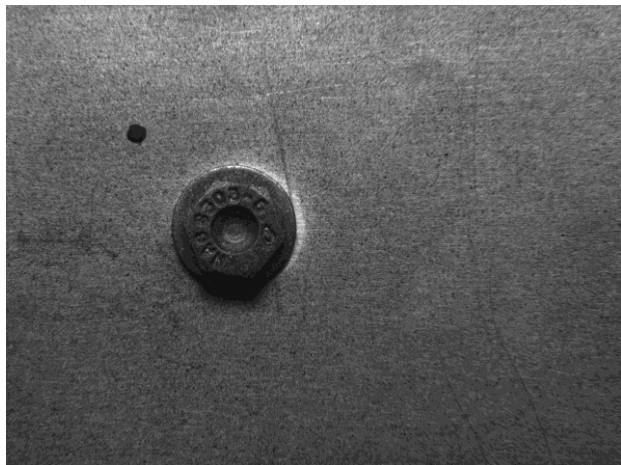
(a.1)   **(b.1)**
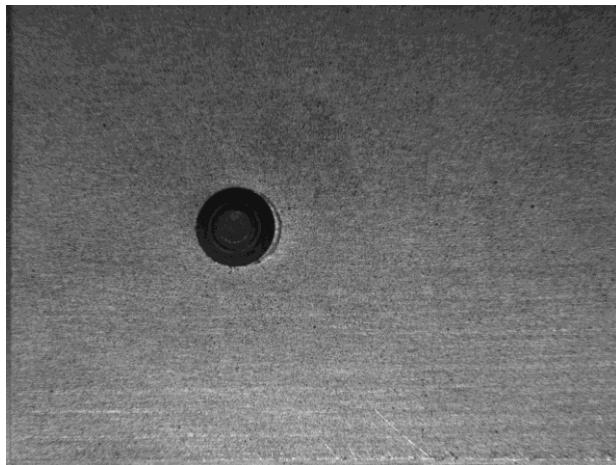
(a.2)   **(b.2)**

Figure 18: Images of both sides of one of the joints of specimen DIC 02 captured at (a.1) and (b.1) 3.2 kip (sixth cycle peak load), and (a.2) and (b.2) 4.2 kip (seventh cycle peak load).

The location of the self-locking nut and the bolt head/washer can easily be indentified near the center of Figures 19 and 20, respectively. The robustness of the DIC technique can be amply corroborated from Figures 19(b.1) and 20(b.1) in which the displacement of both the bolt end and the bolt head, respectively, is still captured even though the quality of the artificial speckled–pattern generated on before the experiment is reduced by the darker texture of the bolt. In general the measurements corresponding to the area occupied by the bolt/self–locking nut and the bolt head were disregarded.
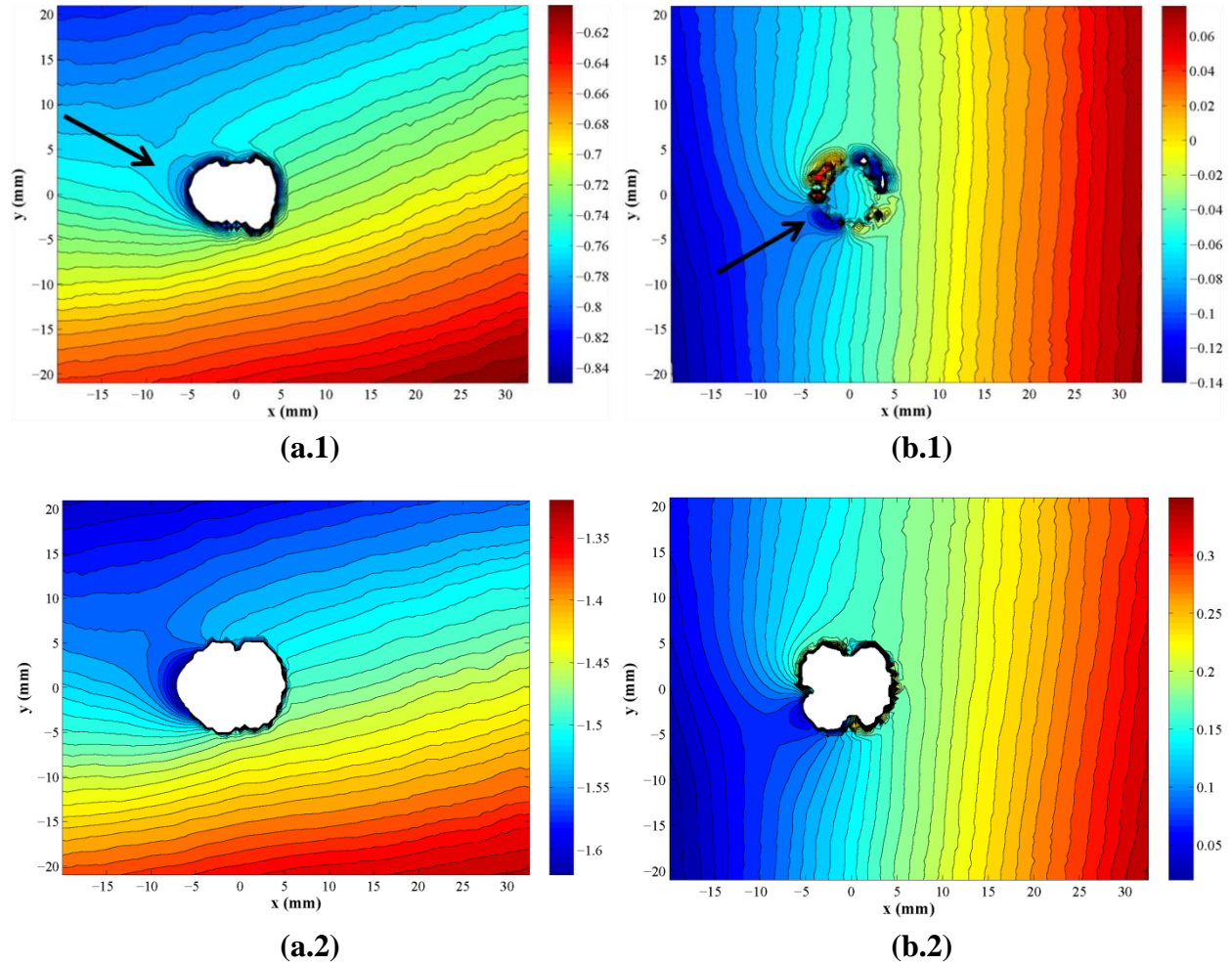
Figure 19: Contour plots of DIC in–plane displacement components (a) x −direction and (b) y −direction measured from the self-locking nut side of one of the joints of specimen DIC 02 at load levels of (a.1) and (b.1) $3.2\ kip$ and (a.2) and (b.2) $4.2\ kip$.

When examining Figures 19 and 20, it can be seen that the areas corresponding to the self–locking nut and the bolt head have been enlarged, this is a direct result of the bearing load generated by the bolt shank upon the lateral surface of the hole of the doublers. This is more pronounced on the self–locking nut side of the joint. The extent of the area of contact between the bolt shank and the lateral surface of the hole of the surface could also be determined. For instance, the approximate limits of the contact area on the self-locking nut side for an applied load of 3.2 kip are shown with arrows in Figures 19 a.1 and b.1. Similar estimations could be obtained from Figure 20. It is quite obvious that this area is symmetric with respect to the negative x axis (*i.e.*, $\theta = \pm 180°$). Finally, Figures 19 and 20 give a very good idea of both the location and extent of the localized plastic deformation around the joint.

Since the measured in-plane displacement distribution includes rigid body translation and rotation, it cannot be used to predict failure. In this case the in-plane strain distribution needs to be determined. As mentioned above, the DIC technique not only measures the in-plane displacement field but also the in–plane strain field. However, the small gage lengths used in the

24

correlation induces a poor signal–to–noise ratio resulting in much less accurate strain distribution measurements. To overcome this problem, there exist two approaches: (*i*) reduce the noise directly from the strain distribution measured by the DIC technique or (*ii*) first reduce the noise from the displacement field and then use it to estimate the strain fields. In this investigation, the latter approach was utilized and is described in the next sub-section.

(a.1)

(b.1)

(a.2)

(b.2)
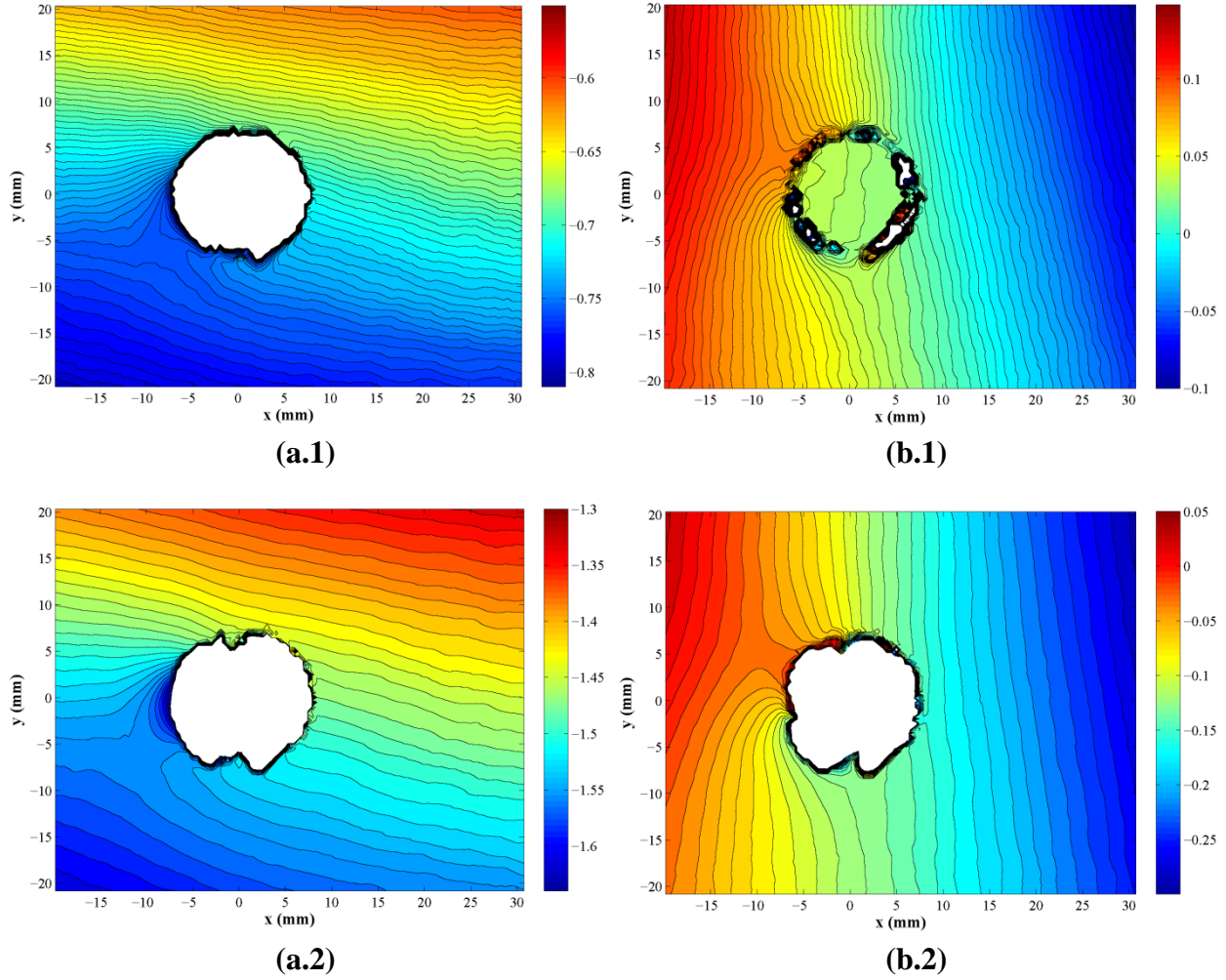
Figure 20: Contour plots of DIC in–plane displacement components (a) $x-$direction and (b) $y-$direction measured from the bolt head of one of the joints of specimen DIC 02 at load levels of (a.1) and (b.1) $3.2\ kip$ and (a.2) and (b.2) $4.2\ kip$.

4.2.1.2 In-plane Strains

Several procedures to reduce noise can be found in the literature [17,18]. In this investigation, the one proposed by Lanza di Scalea *et al.* [18] was implemented. In this approach, the displacement field measured by the DIC technique is *locally* smoothed by applying a least squares surface-fitting method over a subset taken from the DIC measured displacement distribution. Let the dimension of a subset be $n \times n$ and its components be the values of the components of the DIC displacement in the $x-$ and $y-$direction u_{kl} and v_{kl}, respectively; and

the corresponding spatial coordinates (x_{kl}, y_{kl}), where $k, l = 1, 2, \cdots, n$ (n must be an odd integer). Assuming that the in-plane displacement components over the subset can be effectively represented by the following expressions

$$u(x, y) = a_1 x + b_1 y + c_1 \tag{3a}$$

$$v(x, y) = a_2 x + b_2 y + c_2 \tag{3b}$$

then the in-plane components of the strain tensor can be estimated as follows

$$\varepsilon_x = \frac{\partial u}{\partial x} = a_1 \tag{4a}$$

$$\varepsilon_y = \frac{\partial v}{\partial y} = b_2 \tag{4b}$$

$$\varepsilon_{xy} = \frac{1}{2}\left(\frac{\partial u}{\partial y} + \frac{\partial v}{\partial x}\right) = \frac{1}{2}(b_1 + a_2) \tag{4c}$$

Therefore the strain estimation reduces to finding the constant coefficients of $u(x, y)$ and $v(x, y)$ by minimizing the following expressions

$$S_u = \sum_{k=1}^{n}\sum_{l=1}^{n}[u(x_{kl}, y_{kl}) - u_{kl}]^2 = \sum_{k=1}^{n}\sum_{l=1}^{n}[a_1 x_{kl} + b_1 y_{kl} + c_1 - u_{kl}]^2 \tag{5a}$$

$$S_v = \sum_{k=1}^{n}\sum_{l=1}^{n}[v(x_{kl}, y_{kl}) - v_{kl}]^2 = \sum_{k=1}^{n}\sum_{l=1}^{n}[a_2 x_{kl} + b_2 y_{kl} + c_2 - v_{kl}]^2 \tag{5b}$$

To minimize these expressions, their partial derivatives with respect to the coefficients must be set to zero. The minimization of S_u is outlined below

$$\frac{\partial S_u}{\partial a_1} = 2a_1 \sum_{k=1}^{n}\sum_{l=1}^{n} x_{kl}^2 + 2b_1 \sum_{k=1}^{n}\sum_{l=1}^{n} x_{kl}y_{kl} + 2c_1 \sum_{k=1}^{n}\sum_{l=1}^{n} x_{kl} - 2\sum_{k=1}^{n}\sum_{l=1}^{n} u_{kl}x_{kl} = 0 \tag{6a}$$

$$\frac{\partial S_u}{\partial b_1} = 2a_1 \sum_{k=1}^{n}\sum_{l=1}^{n} x_{kl}y_{kl} + 2b_1 \sum_{k=1}^{n}\sum_{l=1}^{n} y_{kl}^2 + 2c_1 \sum_{k=1}^{n}\sum_{l=1}^{n} y_{kl} - 2\sum_{k=1}^{n}\sum_{l=1}^{n} u_{kl}y_{kl} = 0 \tag{6b}$$

$$\frac{\partial S_u}{\partial c_1} = 2a_1 \sum_{k=1}^{n}\sum_{l=1}^{n} x_{kl} + 2b_1 \sum_{k=1}^{n}\sum_{l=1}^{n} y_{kl} + 2n^2 c_1 - 2\sum_{k=1}^{n}\sum_{l=1}^{n} u_{kl} = 0 \tag{6c}$$

In order to solve simultaneously the previous three equations, it is better to arrange them in matrix form

$$
\begin{bmatrix}
\sum_{k=1}^{n}\sum_{l=1}^{n} x_{kl}^2 & \sum_{k=1}^{n}\sum_{l=1}^{n} x_{kl}y_{kl} & \sum_{k=1}^{n}\sum_{l=1}^{n} x_{kl} \\
\sum_{k=1}^{n}\sum_{l=1}^{n} x_{kl}y_{kl} & \sum_{k=1}^{n}\sum_{l=1}^{n} y_{kl}^2 & \sum_{k=1}^{n}\sum_{l=1}^{n} y_{kl} \\
\sum_{k=1}^{n}\sum_{l=1}^{n} x_{kl} & \sum_{k=1}^{n}\sum_{l=1}^{n} y_{kl} & n^2
\end{bmatrix}
\begin{Bmatrix} a_1 \\ b_1 \\ c_1 \end{Bmatrix}
=
\begin{Bmatrix}
\sum_{k=1}^{n}\sum_{l=1}^{n} u_{kl}x_{kl} \\
\sum_{k=1}^{n}\sum_{l=1}^{n} u_{kl}y_{kl} \\
\sum_{k=1}^{n}\sum_{l=1}^{n} u_{kl}
\end{Bmatrix}
\tag{7}
$$

In similar fashion, the minimization of S_v yields

$$
\begin{bmatrix}
\sum_{k=1}^{n}\sum_{l=1}^{n} x_{kl}^2 & \sum_{k=1}^{n}\sum_{l=1}^{n} x_{kl}y_{kl} & \sum_{k=1}^{n}\sum_{l=1}^{n} x_{kl} \\
\sum_{k=1}^{n}\sum_{l=1}^{n} x_{kl}y_{kl} & \sum_{k=1}^{n}\sum_{l=1}^{n} y_{kl}^2 & \sum_{k=1}^{n}\sum_{l=1}^{n} y_{kl} \\
\sum_{k=1}^{n}\sum_{l=1}^{n} x_{kl} & \sum_{k=1}^{n}\sum_{l=1}^{n} y_{kl} & n^2
\end{bmatrix}
\begin{Bmatrix} a_2 \\ b_2 \\ c_2 \end{Bmatrix}
=
\begin{Bmatrix}
\sum_{k=1}^{n}\sum_{l=1}^{n} v_{kl}x_{kl} \\
\sum_{k=1}^{n}\sum_{l=1}^{n} v_{kl}y_{kl} \\
\sum_{k=1}^{n}\sum_{l=1}^{n} v_{kl}
\end{Bmatrix}
\tag{8}
$$

If we consider a local coordinate system having its origin at the center of the $n \times n$ subset, it can be shown that the following terms in Eqs. (7) and (8) vanish

$$
\sum_{k=1}^{n}\sum_{l=1}^{n} x_{kl}y_{kl} = \sum_{k=1}^{n}\sum_{l=1}^{n} x_{kl} = \sum_{k=1}^{n}\sum_{l=1}^{n} y_{kl} = 0
\tag{9}
$$

Using Eq. (8), the coefficients vector in Eqs. (6) and (7) can easily be determined and then substituting them into Eqs. (5a) − (5c), the in-plane strains at the center of the $n \times n$ subset are obtained as follows

$$
\varepsilon_x = \frac{\partial u}{\partial x} = a_1 = \frac{\sum_{k=1}^{n}\sum_{l=1}^{n} u_{kl}x_{kl}}{\sum_{k=1}^{n}\sum_{l=1}^{n} x_{kl}^2}
\tag{10a}
$$

$$
\varepsilon_y = \frac{\partial v}{\partial y} = b_2 = \frac{\sum_{k=1}^{n}\sum_{l=1}^{n} v_{kl}y_{kl}}{\sum_{k=1}^{n}\sum_{l=1}^{n} y_{kl}^2}
\tag{10b}
$$

$$
\varepsilon_{xy} = \frac{1}{2}\left(\frac{\partial u}{\partial y} + \frac{\partial v}{\partial x}\right) = \frac{1}{2}(b_1 + a_2) = \frac{1}{2}\left(\frac{\sum_{k=1}^{n}\sum_{l=1}^{n} u_{kl}y_{kl}}{\sum_{k=1}^{n}\sum_{l=1}^{n} y_{kl}^2} + \frac{\sum_{k=1}^{n}\sum_{l=1}^{n} v_{kl}x_{kl}}{\sum_{k=1}^{n}\sum_{l=1}^{n} x_{kl}^2}\right)
\tag{10c}
$$

Figure 21 shows, in the form of contour plots, the results of applying the least squares minimization scheme described above to the in-plane displacement field measured by DIC technique upon both sides of one of the joints of specimen DIC 02 subjected to the peak load of the sixth cycle, $3.2\ kip$. The components of the in-plane displacement fields on both sides of the joint were presented in Figures 19(a.1), (b.1), and 20(a.1), (b.1). Figures 21 (a.1–3) the distribution of in-plane strains ε_x, ε_y and ε_{xy}, respectively, on the self-locking nut side of the joint and Figures 21(b.1–3) show the distribution of the corresponding in-plane strain components upon the bolt head side of the joint. Different subset dimensions were considered, convergence was obtained with a 15×15 subset which corresponds to a gage length of $7.86mm$. It was determined, during the validation process, that in-plane strain levels calculated using the least squares surface-fitting minimization have an error of $\pm\ 200$ microstrains. In addition, the application of the minimization scheme reduces the region of interest, which was used in the digital image correlation, to $(n-1)$ pixels along both the $x-$ and $y-$direction. That is why, the regions shown in Figure 21, are $7.64mm$ smaller than the ones shown in Figures 19 and 20. In the same manner, the diameter of the surfaces representing both the self-locking nut and the bolt head/washer is increased in the same amount. Figure 21 gives very good qualitative information about the distribution of the in–plane strains in the region of the joint. It can be seen that (i) largest strains (positive or negative) occur on the left side of the xy plane (bearing load effect), (ii) normal strains ε_x and ε_y are symmetric with respect to the x–axis while ε_{xy} is skew–symmetric, and (iii) as expected the path of the maximum shear strain $\left(\varepsilon_{xy}\right)_{max}$ occurs along the path where both ε_x and ε_y are zero.
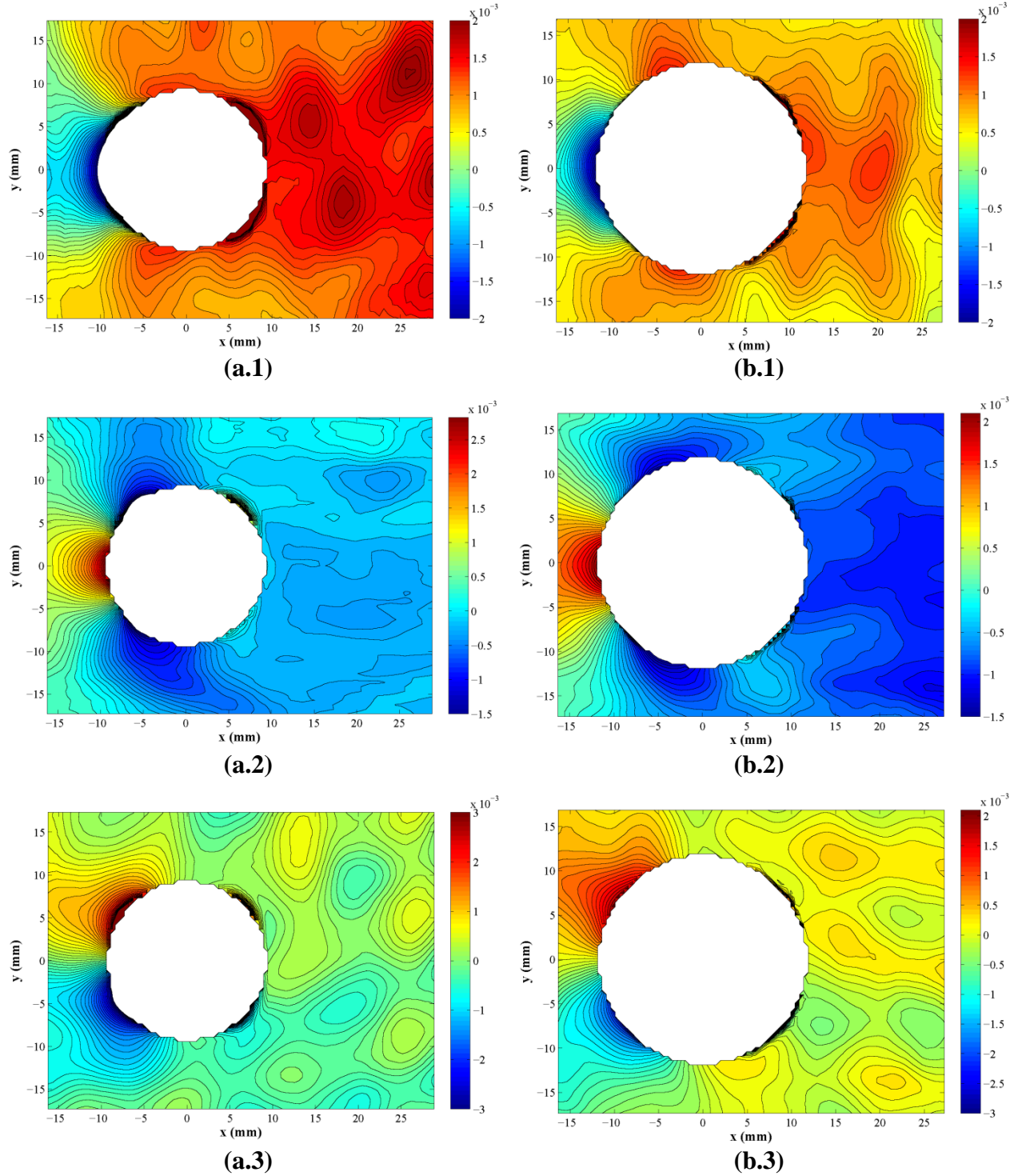
Figure 21: Calculated in-plane strain fields (1) ε_x (2) ε_y and (3) ε_{xy} over (a) the self-locking nut and (b) the bolt head side of a joint of specimen DIC 02 subjected to a peak load $3.2\ kip$ (sixth cycle)

In order to understand the mechanical response of the specimen joint to the applied load, the distribution of the in–plane strain components around each side of one of the joints of specimen

DIC 02 (50 $in \cdot lb$) were calculated at the peak load of every loading cycle (see Figure 6) using the minimization process outlined above. Similar contour plots to the ones presented in Figure 21 were obtained at every loading level and the results are summarized in Figures 22 and 23. Figure 22 shows, for the case of the self-locking nut side of the joint, the variation of the in–plane strain components ε_x (Figure 22(a)), ε_y (Figure 22(b)) and ε_{xy} (Figure 22(c)) as a function of the radial distance for every peak cyclic load and at four different orientations: (1) $\theta = 0°$, (2) $\theta = 153°$, (3) $\theta = 180°$, and (4) $\theta = -153°$. Figure 23 presents the same information provided in Figure 22 but for the bolt head side of the joint. Upon examination of Figures 22 and 23, it can be seen that (*i*) the three in-plane strain components are minimum at $\theta = 0°$, (*ii*) at $\theta = 180°$, ε_x is maximum in tension, ε_y is maximum in compression, and ε_{xy} is minimum (this is more pronounced on the self-locking nut side), (*iii*) the maximum shear strain $\left(\varepsilon_{xy}\right)_{max}$ occurs at $\theta = \pm153°$ where the normal strains are small, and (*iv*) strain levels is the same at both sides of the joint.

(a.1)

(b.1)

(c.1)
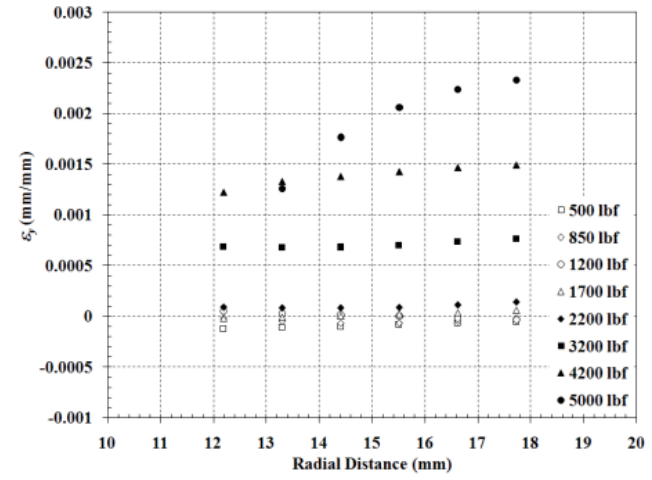
(a.2)
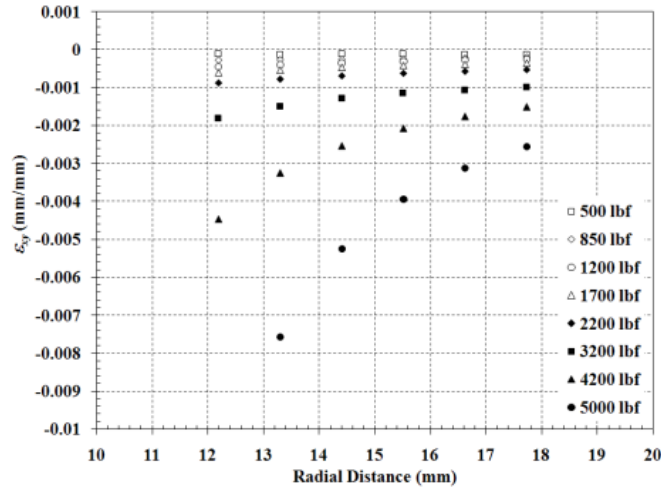

(b.2)

(c.2)

32

(a.3)
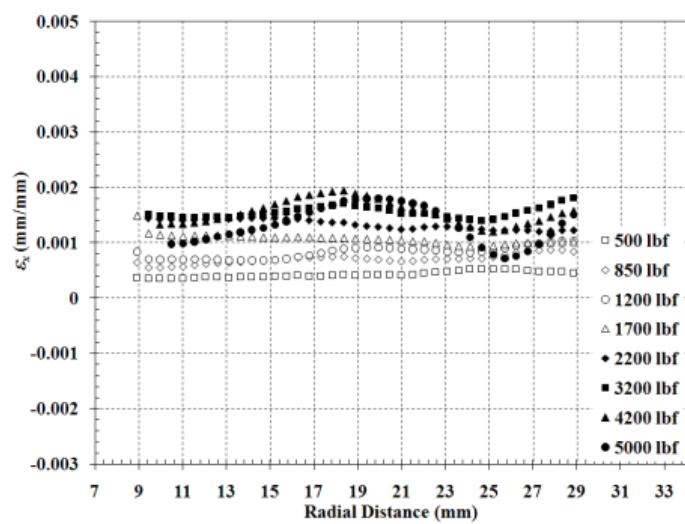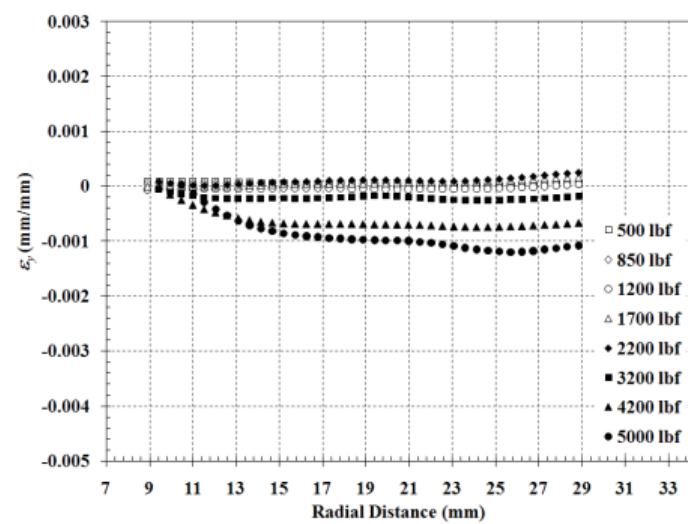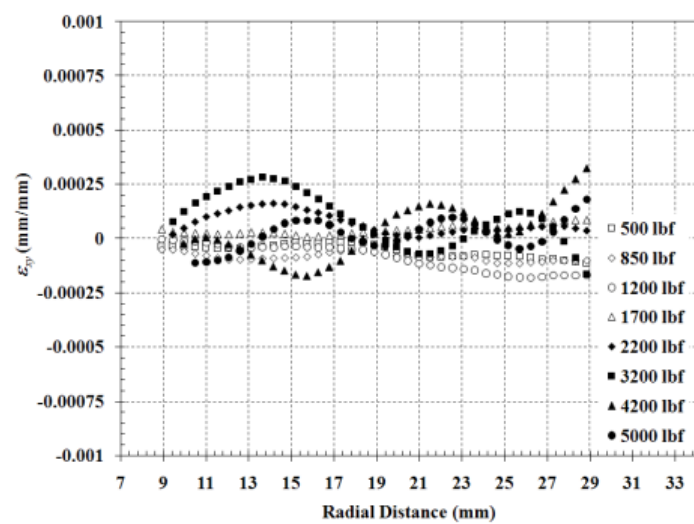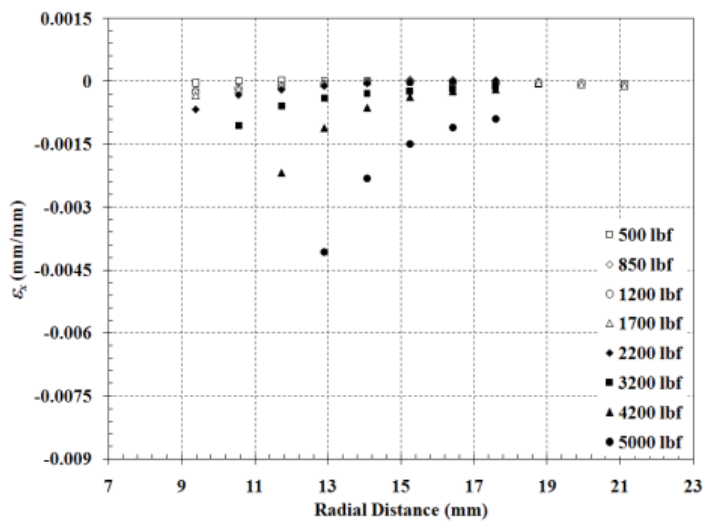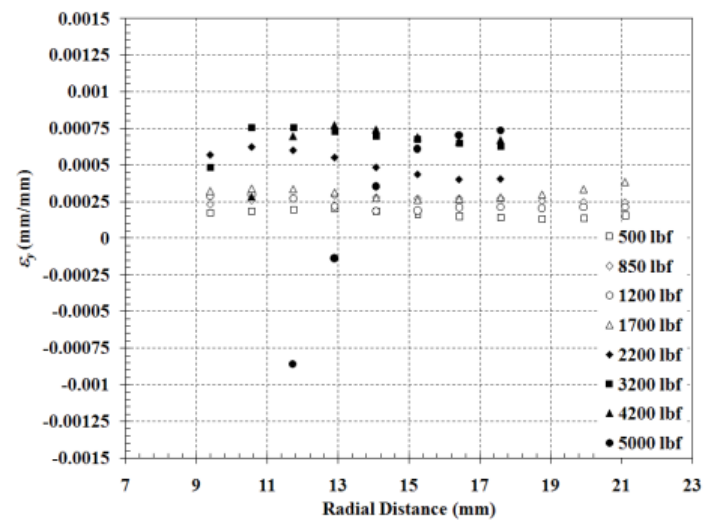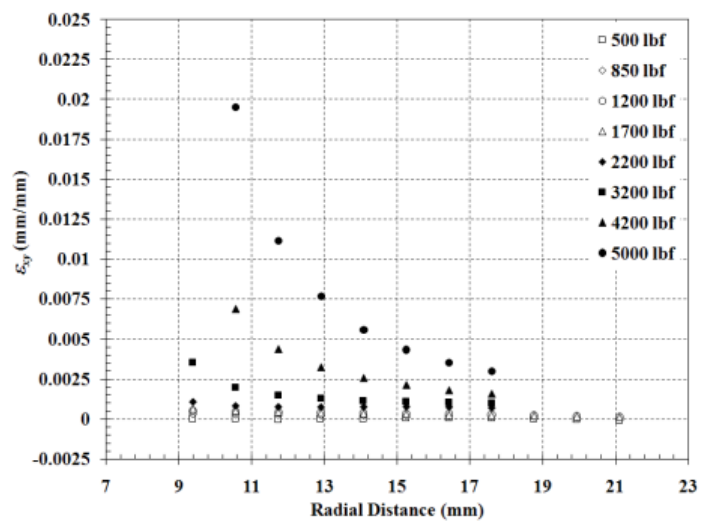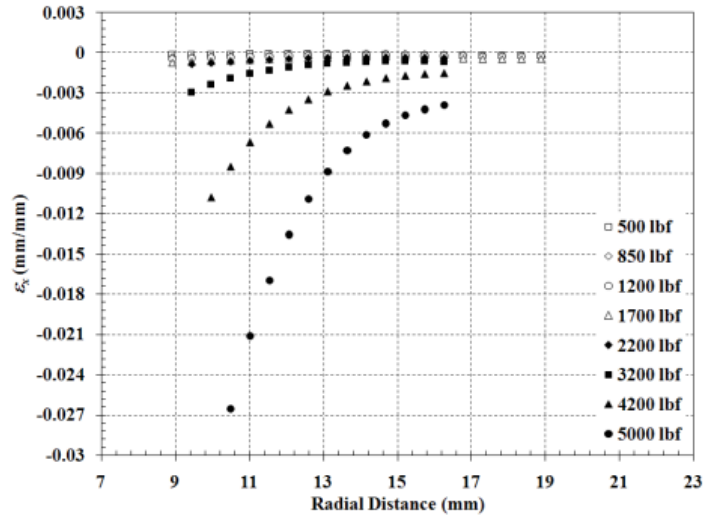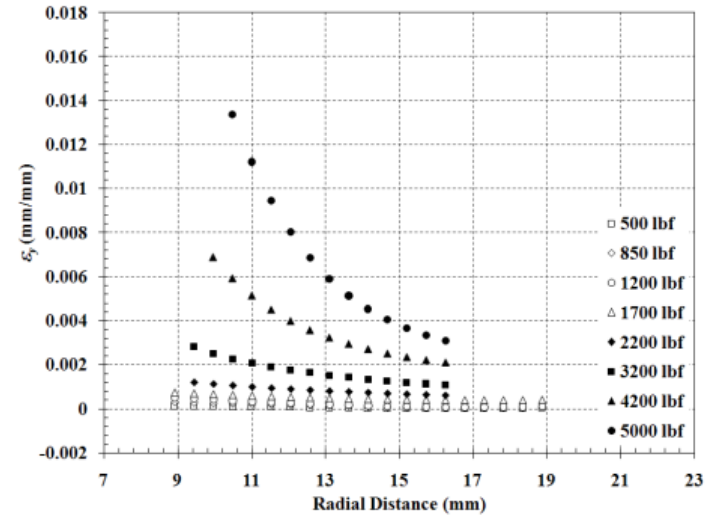
(b.3)
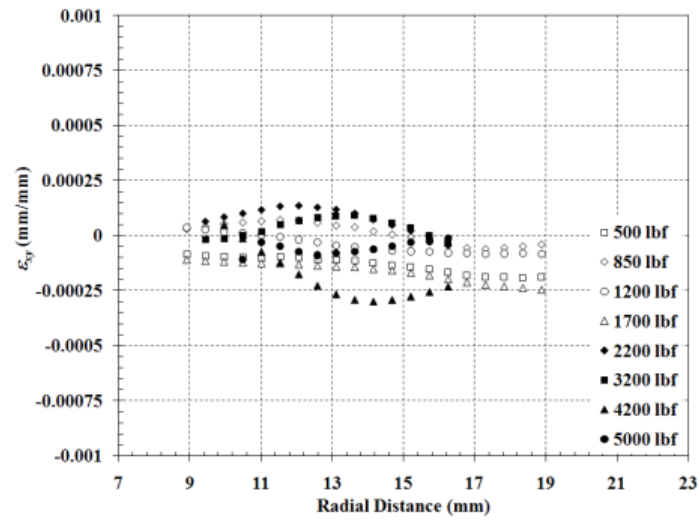

(c.3)
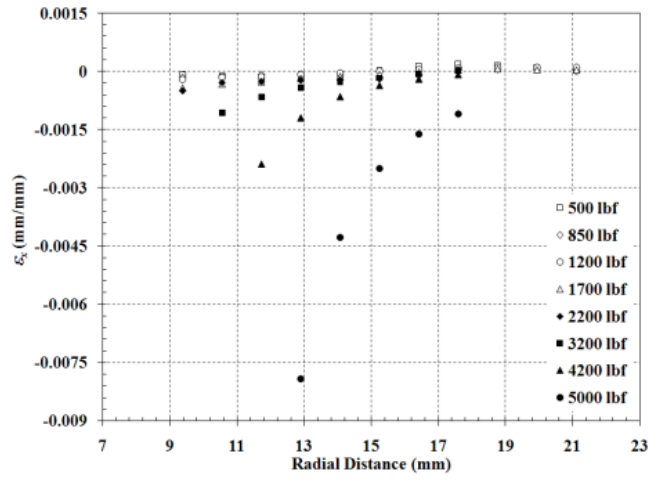
(a.4)
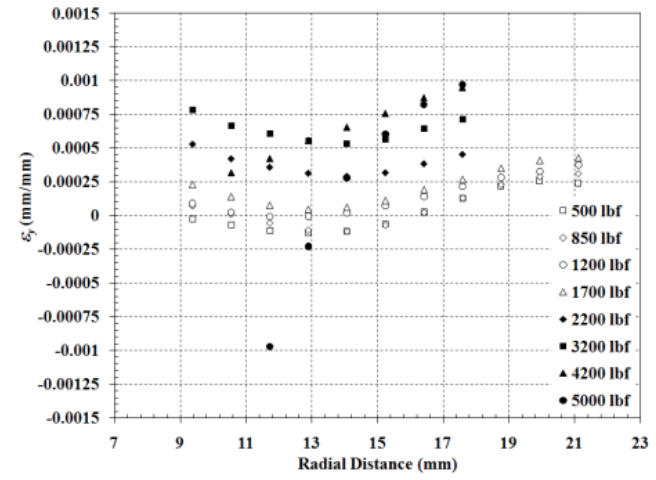
(b.4)
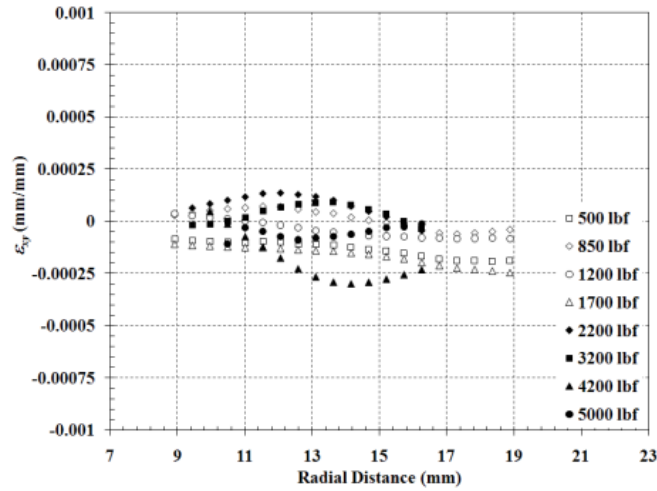
(c.4)

Figure 22: Effect of the applied load (peak of every cycle) upon the radial variation of in–plane strains (a) ε_x (b) ε_y and (c) ε_{xy} at orientations (1) $\theta = 0°$, (2) $\theta = 153°$, (3) $\theta = 180°$, and (4) $\theta = -153°$ on the self-locking nut side of a joint of specimen DIC 02 (error: ± 200 µstrains)

(a.1)

(b.1)

(c.1)

(a.2)

(b.2)

(c.2)

36

(a.3)

(b.3)

(c.3)
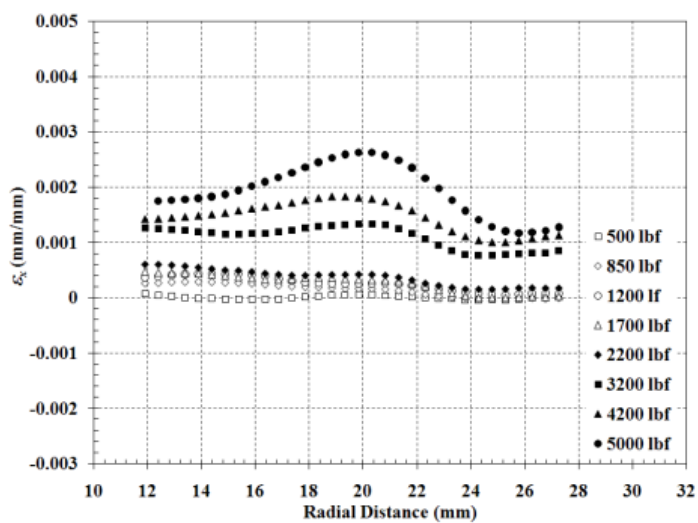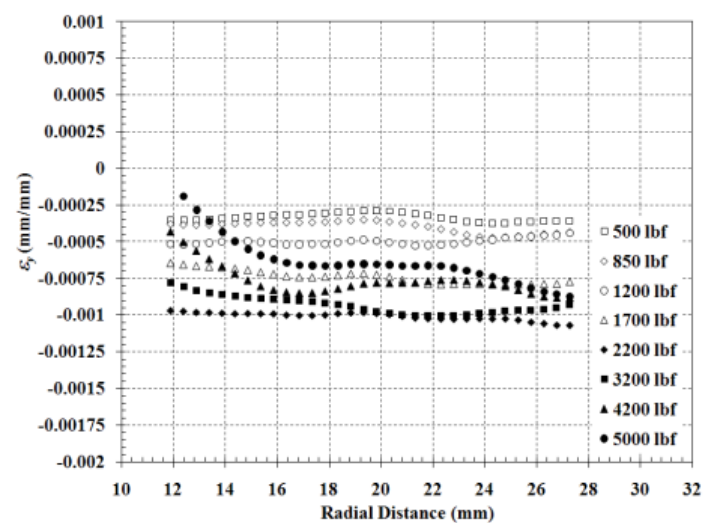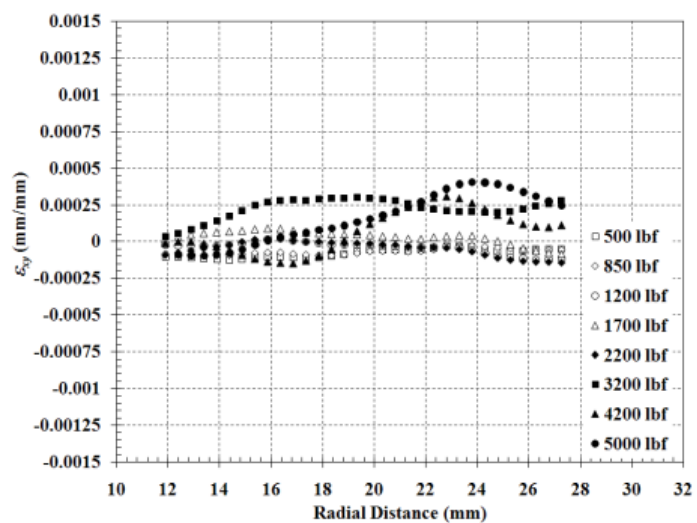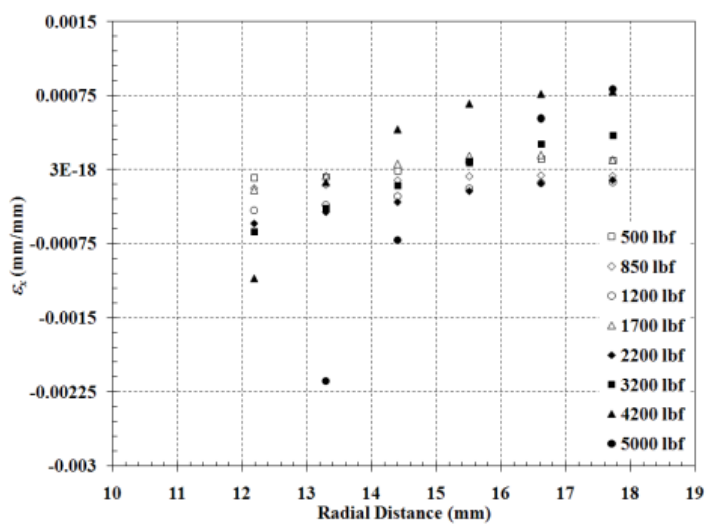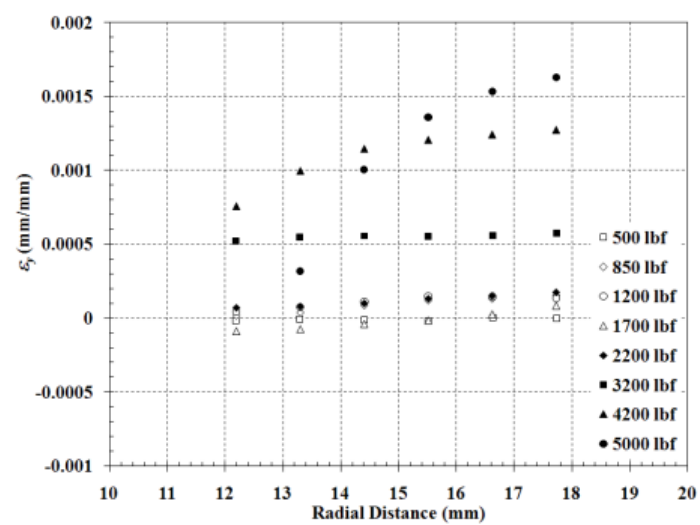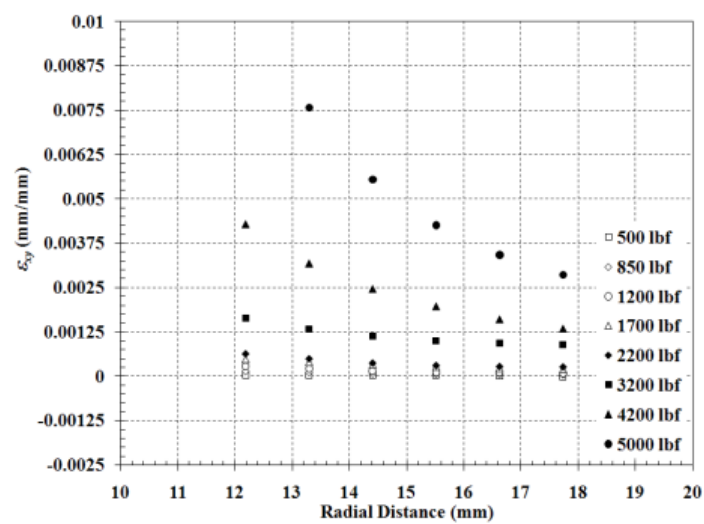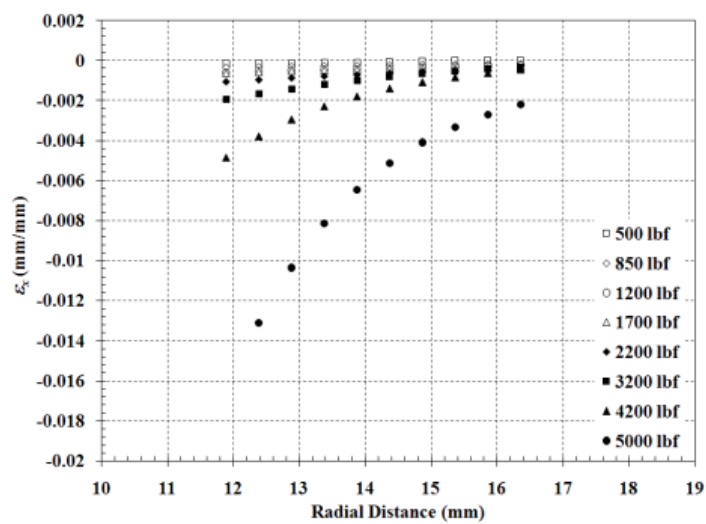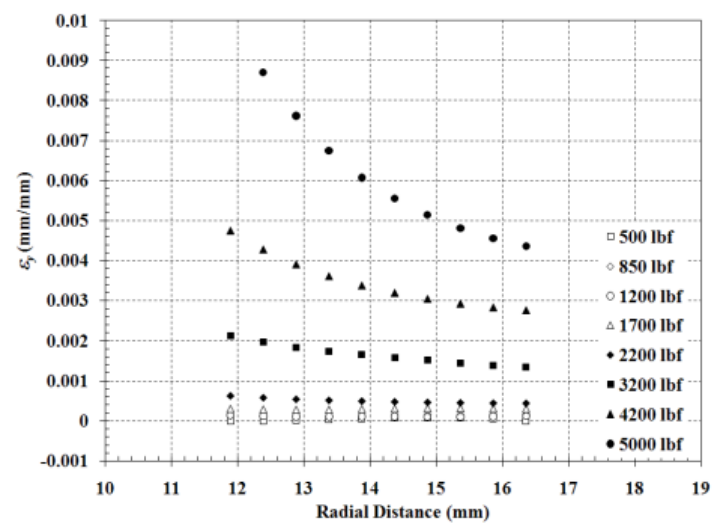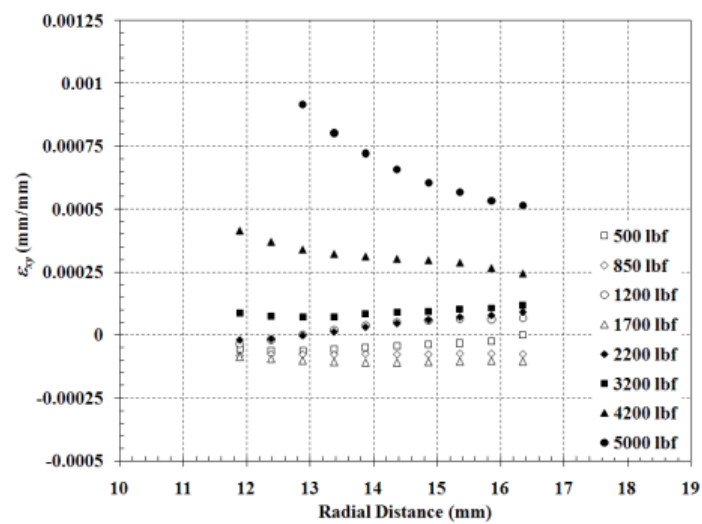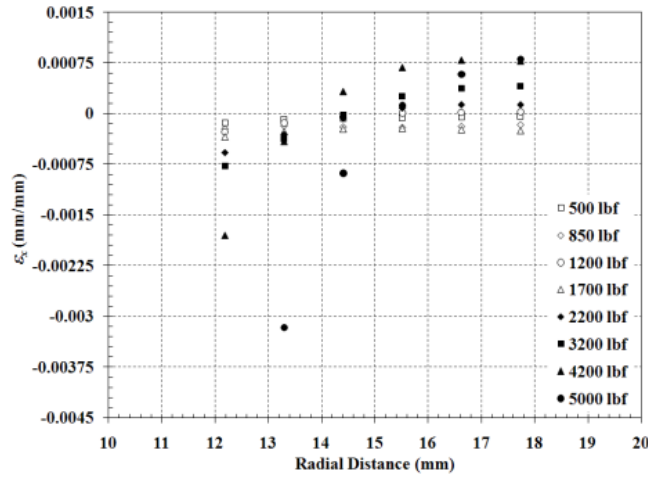
Figure 23: Effect of the applied load (peak of every cycle) upon the radial variation of in–plane strains (a) ε_x (b) ε_y and (c) ε_{xy} at orientations (1) $\theta = 0°$, (2) $\theta = 153°$, (3) $\theta = 180°$, and (4) $\theta = -153°$ on bolt head side of a joint of specimen DIC 02 (error: ±200 µstrains)

4.2.2 TSA Results

As mentioned previously, in the TSA experiments the adiabatic conditions required by this technique were only obtained at the valley and peak of each loading cycle after applying the oscillating load of ± 50 lb at 8 Hz. In all the cases, the distribution of temperature change over the region of interest measured by this technique included extraneous noise. To reduce this noise, a mean filter, which assigns each pixel a new value equal to the mean of its original value and those of the surrounding eight pixels, was used. Figure 24 shows the filtered temperature change distribution (in ºC) around the self-locking nut of the joint of specimen TSA 05 at every cycle peak. The noise in the TSA raw data is obvious from Figure 24(c) (3rd cycle) where it can be seen that not even the mean filter was able to remove the noise from the actual measurement. It can be seen from this figure that in all the cases the surface of the doubler located to the left of the self-locking nut undergoes higher temperature changes than the region that is on the right. This is in agreement with the DIC measurements (see Figure 21). Something that might seem surprising from Figure 24 is the fact that the temperature change distribution remains almost invariable at every peak cycle (except the last one) even though the peak load is increased with every cycle. The explanation can be found after examining Equation (1) and remembering the adiabatic conditions required by this technique. Equation (1) states that the change in temperature on the surface of interest depends on the stress amplitude (*i.e.*, the amplitude of the applied load) under adiabatic conditions. Since these conditions were satisfied only at the peak and valley of every cycle and the applied load amplitude was the same at each valley and peak for all the cycles (100 lb), then the temperature change distribution measured by the TSA technique and shown in Figure 24 for specimen TSA 05 should be the same at every peak cycle. Regarding the measurements of the temperature change at the peak load of the 8th cycle that are shown in Figure 24(g), it is obvious that those measurements are not valid, since the TSA measurements are only valid if the applied load is inside the material elastic region, which is not the case in the last cycle of the loading profile.
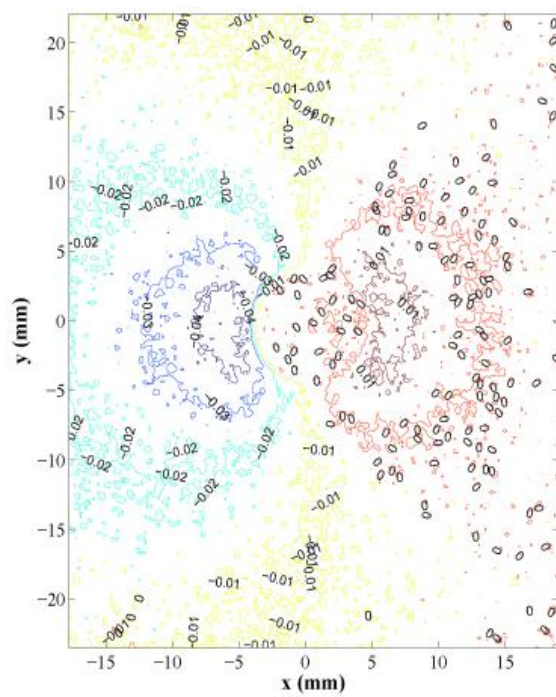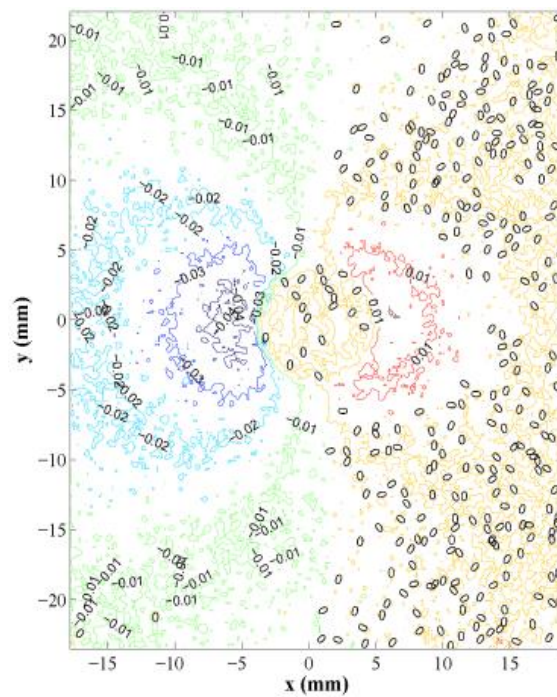
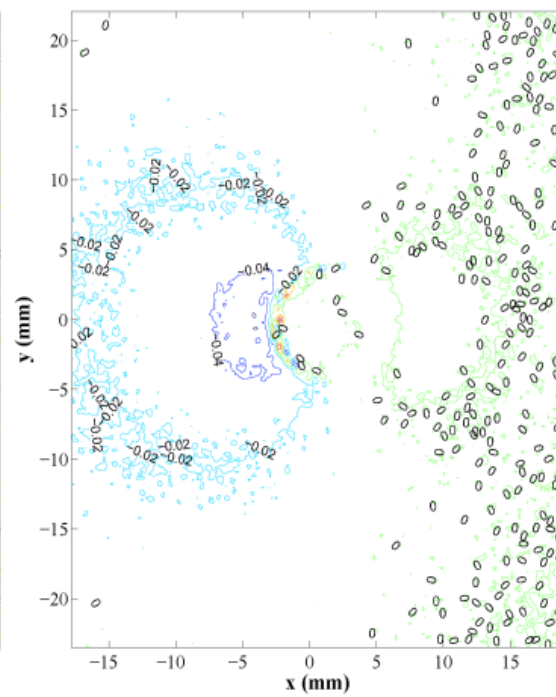**(a)**   **(b)**   **(c)**

40

(d)   **(e)**   **(f)**

41
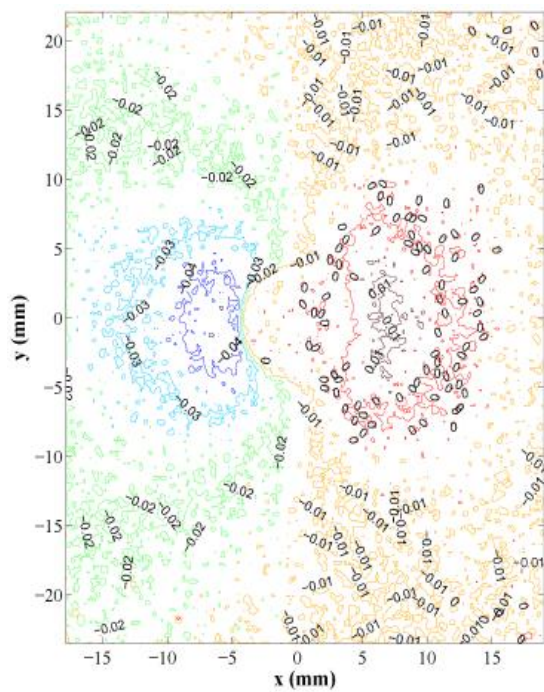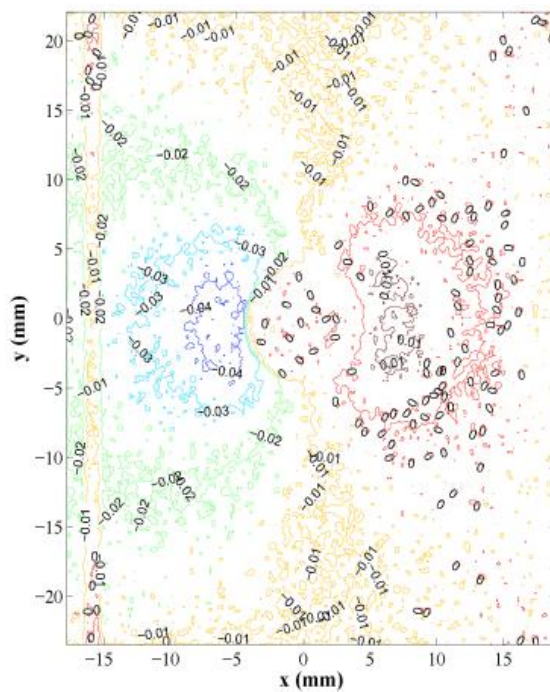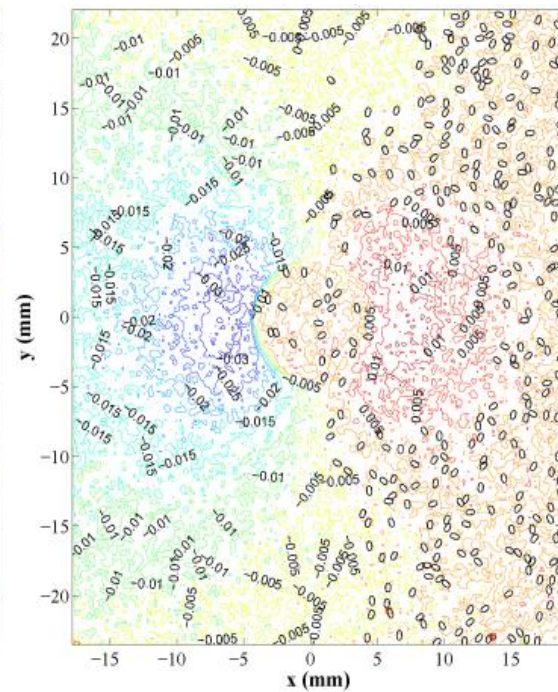
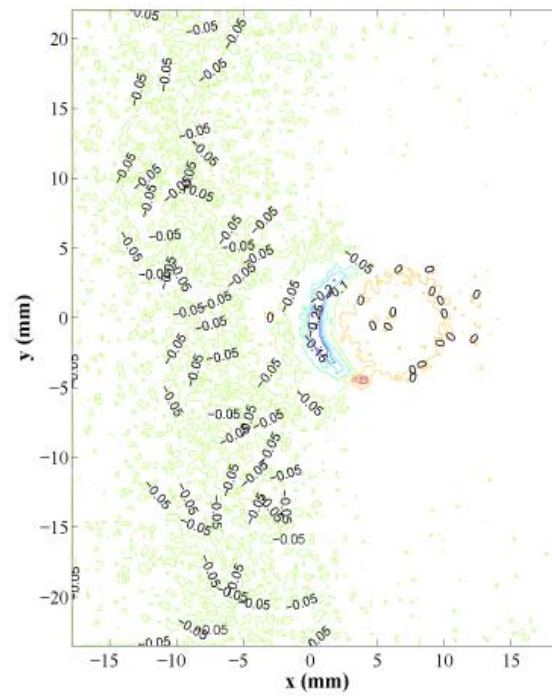**(g)**

Figure 24: Distribution of the change in temperature (in ºC) around the self-locking nut side of the joint measured at the peak load of the each loading cycle: (a) 0.5 kip,
(b) 0.85 kip, (c) 1.2 kip, (d) 1.7 kip, (e) 2.2 kip, (f) 3.2 kip, and (g) 4.2 kip.

4.3 Modeling Results

The finite element model yielded similar results to the DIC technique. Many of the trends seen between the bolt head/washer side and the self-locking nut side were present in the model's results. However, in order to achieve these results, the model went through a series of iterations. Initially the published values for the three coefficients of friction were used [19]. It was surmised that this was creating too many severe discontinuities and the model failed to run. To correct this, the coefficients were dropped to 80% of their published value. The model ran successfully, but the results yielded much lower strains than the DIC results. The coefficients were then dropped to 10% of the published values. This model ran successfully, but the strains were higher than the strains seen in the DIC results. The model continued to be run at varying magnitudes of the coefficients of friction: 35% for all three coefficients, 25% for Al-Al and 35% for Al-Stainless Steel and Al-Zn, 25% for Al-Al, 100% for Al-Stainless Steel, and 90% for Al-Zn, and finally 25% for all three coefficients. The results appeared to be closest to those of the DIC results when all three coefficients were placed at 25% of their published value. The variation in these values can be seen in Table 4.

Table 4: Values of the friction coefficient μ used in the simulations

Contact Surfaces	μ at 100%	μ at 35%	μ at 25%	μ at 10%
Aluminum-Aluminum	1.05	0.3675	0.2625	0.105
Aluminum-Stainless Steel	0.61	0.2135	0.1525	0.061
Aluminum-Zinc	0.85	0.2975	0.2125	0.085

There are several reasons why the coefficients had to be greatly varied to achieve results close to the DIC results. First, the equation used to calculate the bolt load used in the model assumed a correction factor of 0.2. If for some reason, that correction factor differed for these experiments, the applied bolt load would change. Consequently, the friction seen in the model would have been different and could constitute part of the great variation in value. Also, while the torque wrench was calibrated to within +/- 4%, the actual torque could have been lower than expected, causing the model to need a decreased coefficient of friction to compensate for the decrease in the experiments torque. While these are only two possible reasons for why the coefficient of friction had to be adjusted, it was outside of the scope of this project to investigate these reasons further.

To verify that the model mesh was converged, the mesh size was reduced by one half. After analyzing the new mesh structure, it was concluded qualitatively that the solution with the original mesh had converged. Table 5 presents a comparison in percent difference between the two mesh sizes at $\theta = 180°$ for strains in the loading direction of the $50 in \cdot lb$ case. As seen, the percent difference is consistently lower the further away from the hole it gets. As seen in Table 5, percent difference stayed below 20% for all cases, which was considered good enough for mesh convergence.

Table 5: Percent error between mesh sizes for $50\ in \cdot lb$ torque case at $\theta = 180°$

Radial Distance (in)	Error (%)		
	at 2.2 kip	at 3.2 kip	at 4.2 kip
0.28	5.93	8.59	18.31
0.31	2.82	3.34	15.45
0.34	1.58	1.16	3.45
0.37	-6.62	-6.49	-4.94
0.49	-4.87	-4.78	-3.02
0.60	-4.25	-4.39	-3.98
0.75	1.72	1.72	2.13
0.82	0.97	1.09	1.16
0.90	3.91	2.95	2.33
1.00	-0.55	-0.25	0.17

When comparing the results of the simulations with the DIC measurements, the model yielded similar trends in the data. Consistently, however, the model yielded a higher peak strain value than the DIC data. Depending on angle, location from the hole, and peak loading value, the percent difference between the data varied between about 0.2% and 33%. For example, presented in Table 6 is the comparison between the measured normal strains and the ones determined in the simulation at $\theta = 180°$ and at different radial distances from the center of the self-locking nut of specimen DIC 02 at the peak of the 5th, 6th and 7th loading cycle. It can be seen that in most of the cases the error is less that 10%. These results are expected since as shown previously the specimen underwent extensive localized plastic deformation around the joint at higher loads (see Table 3) and since the strains calculated from the DIC measurements are infinitesimal and not finite strains, the large discrepancy between the experimental and simulation results is understandable. Additional plots comparing the DIC results to the model's results can be found in Appendix B.

Table 6: Percent error between the measured and simulation-calculated normal strains

X - in	% diff 2.2 kip	% diff 3.2 kip	% diff 4.2 kip
0.310811	21.61	-1.75	5.03
0.341727	32.93	-5.17	-0.48
0.372642	7.05	12.40	-3.40
0.488498	-8.62	16.90	14.00

5.0 CONCLUSIONS AND RECOMMENDATIONS

In this investigation the digital image correlation (DIC) and the thermoelastic stress analysis (TSA) techniques were used to measure the mechanical response around a mechanically fastened joint subjected to varying amplitude cyclic loading. An FEM model was also created in ABAQUS/CAE to compare with the experimental results and extract additional parameters such as friction coefficients between surfaces that are very difficult to measure during the experiments. The DIC and TSA are full-field techniques that measure different physical quantities and specific testing conditions. The DIC measures the in-plane displacement distribution over the region of interest, which can easily be related to in-plane strains. The TSA measures the temperature change over the same region which can be related to the sum of the change on the in-plane principal stresses. The DIC technique requires a random speckle-pattern on the surface, while the TSA requires adiabatic conditions and a surface with high and uniform radiation emissivity. The specific requirements of each technique were carefully satisfied. From the analysis of the results we can conclude the following:

a) The DIC technique measured accurately the distribution of the in-plane displacement over the region surrounding the joint.
b) It has been shown in other investigations (see for example [20]) that the DIC technique can directly measure the in-plane strain distribution when the signal-to-noise ratio is very small. In this investigation the measured in-plane strain distribution was noisy, so a least-squares minimization was applied to the measured in-plane displacement to obtain the in-plane strain distribution. The calculated in-plane distribution provided the location of regions subjected to higher levels of strain, which agreed with the post-mortem observations on the tested specimens.
c) The information provided by the TSA technique was minimal. This was due to the way the low-frequency varying-amplitude cyclic loading was applied. This technique requires adiabatic conditions throughout the experiment to successfully measure the temperature change over the surface of interest. Adiabatic conditions can be generated by applying a high-frequency constant-amplitude cycling loading. In the TSA experiments these conditions were met only at the peaks and valleys of the cyclic loading.
d) The FEM model was able to resemble the DIC experiments within an error of less that 6% in strain when the friction coefficients between the different surfaces in contact used in the simulations was reduced to 25% of their published values.

Based on these conclusions, two recommendations can be presented. First, the DIC worked very well in this experiment and should be used in the future as a full field measurement technique. However, it is important to verify all results. In this case, the DIC results showed the location of high strain areas. A strain gage could have been fixed to one of these areas to verify the DIC results. This could have been accomplished in just one or two additional test runs, but would have added to the validity of the results. Second, it is recommended that the TSA technique be avoided for quasi-static loading experiments.

Also, recall that the key performance parameters were a computer model accurate to within 70% of the stress near the hole, and a comparison between the DIC and TSA results with accuracy within +/- 500psi. Due to the lack of results from the TSA experiments, the comparison between

the DIC and TSA results could not occur. For the computer model, it was only accurate to within 70% of the strain near the hole once the coefficients of friction were adjusted. With continued research and use, DIC will be an excellent full-field technique for Air Force research.

6.0 References

1. ASTM Standard E8-04, "Standard Test Methods for Tension Testing of Metallic Materials," ASTM International, West Conshohocken, PA, www.astm.org.
2. SAE Aerospace Standard AIR1471, "Torque Tightening Threaded Fasteners," SAE International, Warrendale, PA, www.sae.org.
3. Peters, W.H. and Ranson, W.F., (1982), "Digital Imaging Techniques in Experimental Stress Analysis," Optical Engineering, Vol. 21, No. 3, pp. 427 – 431.
4. Sutton, M.A., Wolters, W.J., Peters, W.H., Ranson, W.F., and McNeill, S.R., (1983), "Determination of Displacements using an Improved Digital Image Correlation Method," Image and Vision Computing, Vol. 1, No. 3, pp. 133 – 139.
5. Vendroux, G. and Knauss, W.G., (1998), "Submicron Deformation Field Measurements: Part 2. Improved Digital Image Correlation," Experimental Mechanics, Vol. 38, No. 2, pp. 86 – 92.
6. Stanley, P. and Chan, W.K., (1985), "Quantitative Stress Analysis by Means of the Thermoelastic Effect," Journal of Strain Analysis, Vol. 20, No. 3, pp. 129 – 137.
7. Oliver, D.E., (1986), "Stress Pattern Analysis by Thermal Emission (SPATE),' Handbook of Experimental Mechanics, Chapter 14, Ed. Kabayashi, A.S., Prentice Hall, Englewood Cliffs, NJ
8. Tong, W., (1997), "Detection of Plastic Deformation Patterns in a Binary Aluminum Alloy," Experimental Mechanics, Vol. 37, No. 4, pp. 452 – 459.
9. Zhang, D., Eggleton, C.D., and Arola, D.D., (2002), Evaluating the Mechanical Behavior of Arterial Tissue using Digital Image Correlation," Experimental Mechanics, Vol. 42, No. 4, pp. 409 – 416.
10. Barthelat, F., Wu, Z., Prorok, B.C., and Espinosa, H.D., (2003), "Dynamic Torsion Testing of Nanocrystalline Coatings using High-speed Photography and Digital Image Correlation," Experimental Mechanics, Vol., 43, No. 3, pp. 331 – 340.
11. Cho, S., Chasiotis, I., Friedmann, T.A., and Sullivan, J.P., (2005), "Young's Modulus, Poisson's Ratio and Failure Properties of Tetrahedral Amorphous Diamond-like Carbon for MEMS Devices,' Journal of Micromechanics and Microengineering, Vol. 15, pp. 728 – 735.
12. Abanto-Bueno, J. and Lambros, J., (2006a), "An Experimental Study of Mixed Mode Crack Initiation and Growth in Functionally Graded Materials," Experimental Mechanics, Vol. 46, pp. 179 – 196.
13. Abanto-Bueno, J. and Lambros, J., (2006b), "Parameters Controlling Fracture Resistance in Functionally Graded Materials under Mode I Loading," International Journal of Solids and Structures, Vol. 43, pp. 3920 – 3939.
14. Abaqus/CEA User's Manual, http://www.simulia.com/support/documentation.html
15. Iancu, F., Ding, Cloud, G.L. and Raju, B.B., (2005), "Three-dimensional Investigation of Thick Single-lap Bolted Joints," Experimental Mechanics, Vol. 45, No. 4, pp. 351 – 358.
16. Barret, Richard T., 1990, "Fastener Design Manual," NASA Reference Publication 1228
17. Creath, K., (1985), "Phase-shifting Speckle Interferometry," Applied Optics, Vol. 24, No. 18, pp. 3053 – 3058.
18. Lanza di Scalea, F., Hong, S.S., and Cloud, G.L., (1997), "Whole-field Strain Measurement in a Pin-loaded Plate by Electronic Speckle Pattern Interferometry and the Finite Element Method," Experimental Mechanics, Vol. 38, No. 1, pp. 55 – 60.
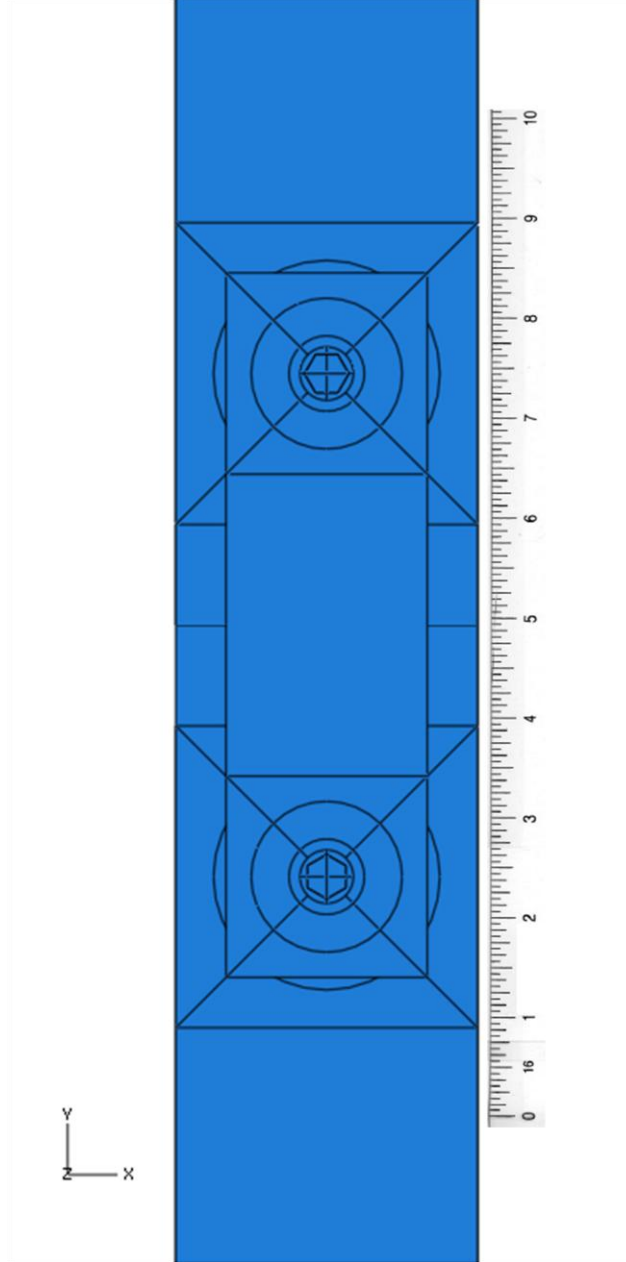
19. Avallone, E.A., Baumeister, T., Sadegh, A., Marks, L.S., (2007), "Friction," <u>Marks' Standard Handbook for Mechanical Engineers,</u> McGraw Hill, New York.
20. Abanto-Bueno, J.L., (2004), "Fracture of a Model Functionally Graded Material Manufactured from a Photo-sensitive Polyethylene," Ph.D. thesis, University of Illinois at Urbana-Champaign.
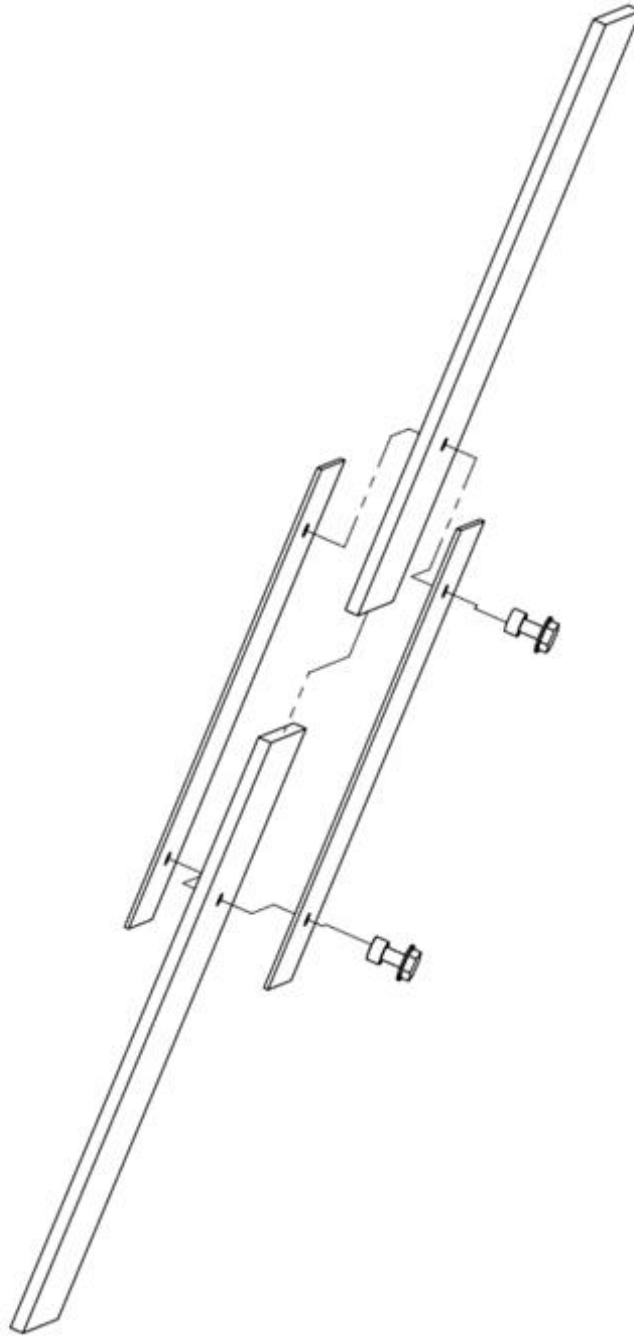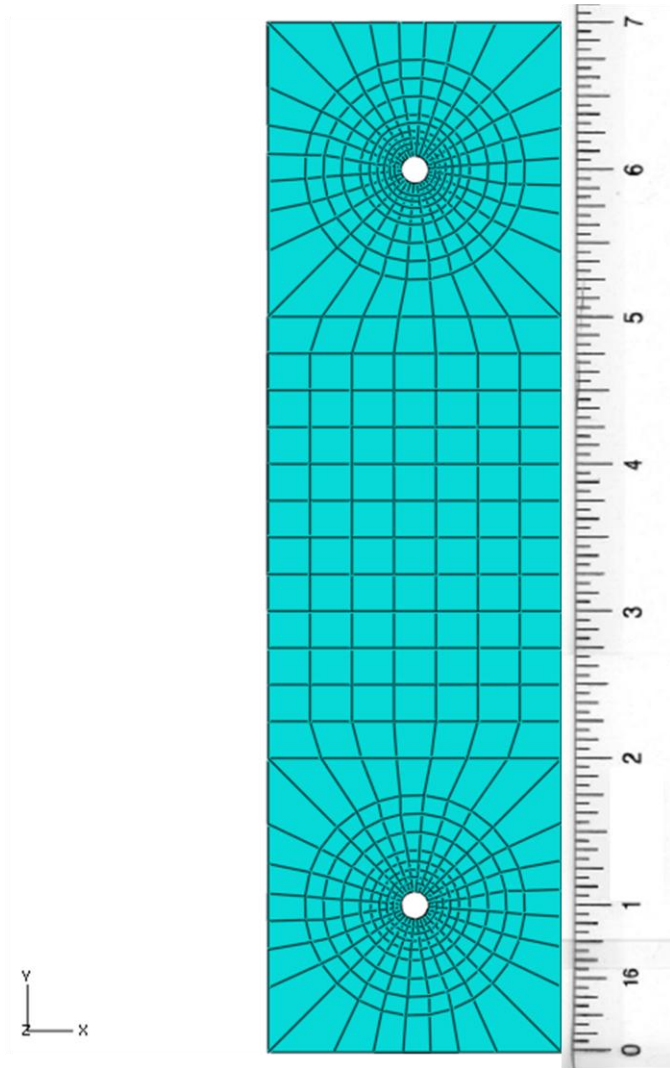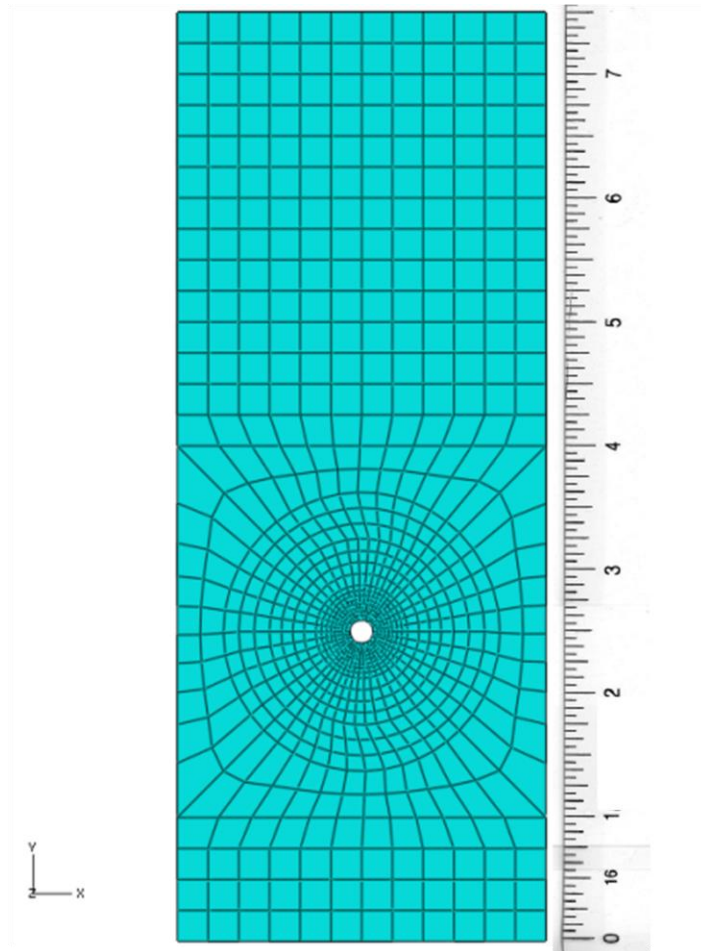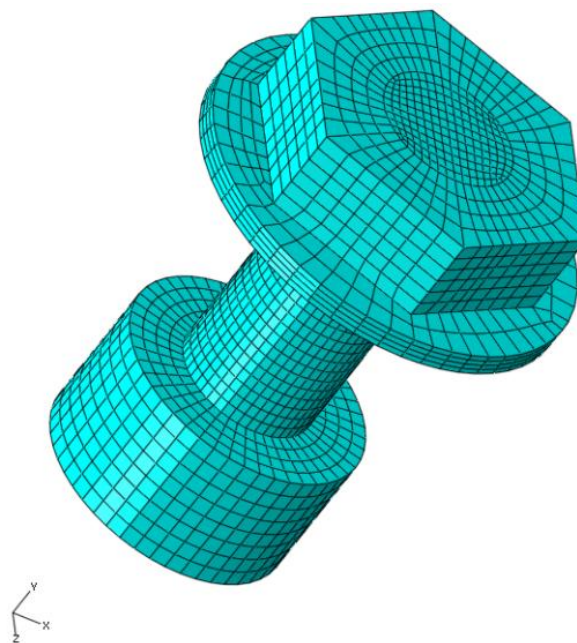
Figure A-1: Exploded view of the test article

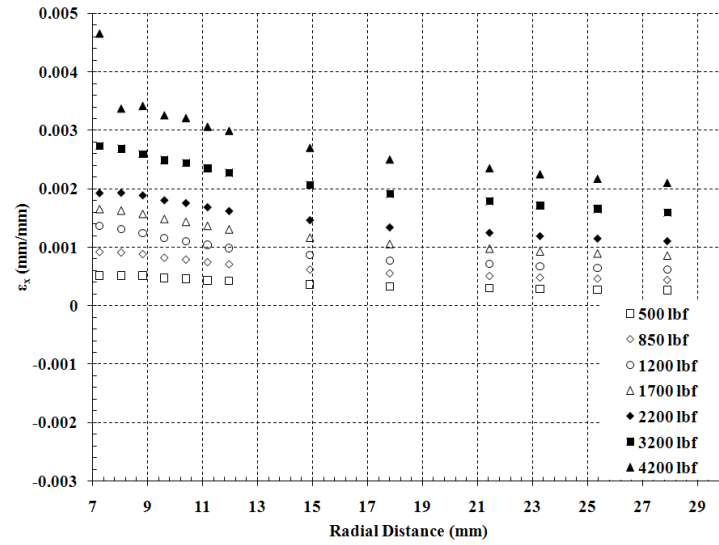**Figure A-2: Assembly with all of the partitions**

Figure A-3: Meshed Doubler

51

Figure A-4: Meshed Central Plate

Figure A-5: Meshed Pin

(a.1)
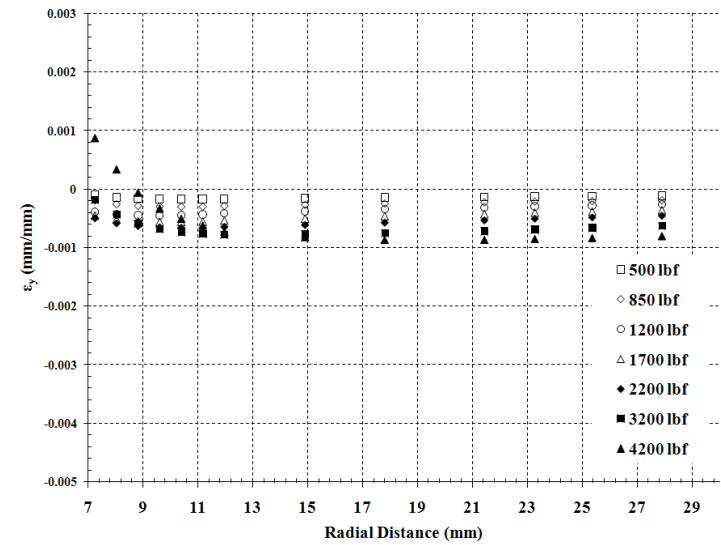
(b.1)

(c.1)

(a.2)

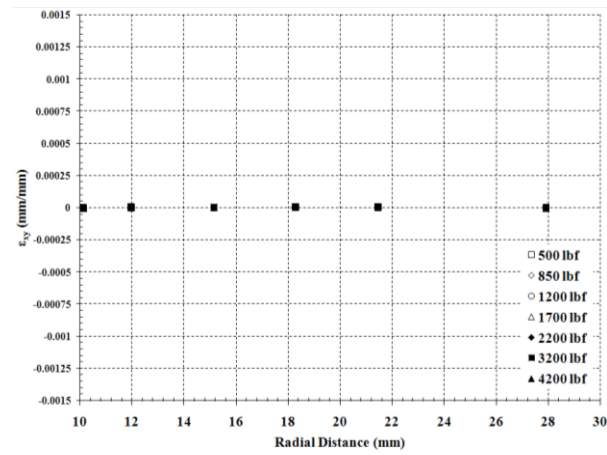(b.2)

(c.2)

(a.3)

(b.3)

(c.3)

(a.4)

(b.4)

(c.4)
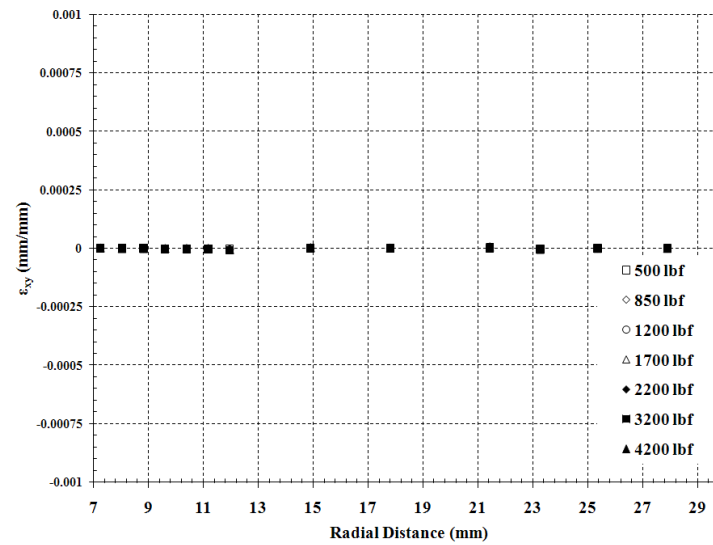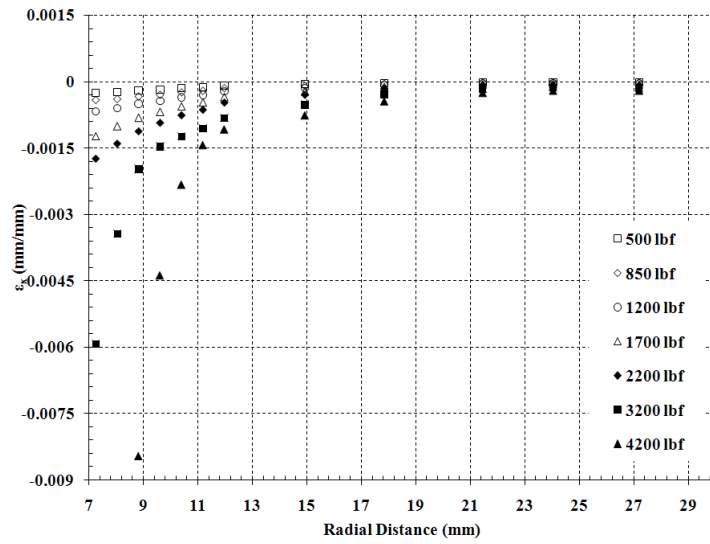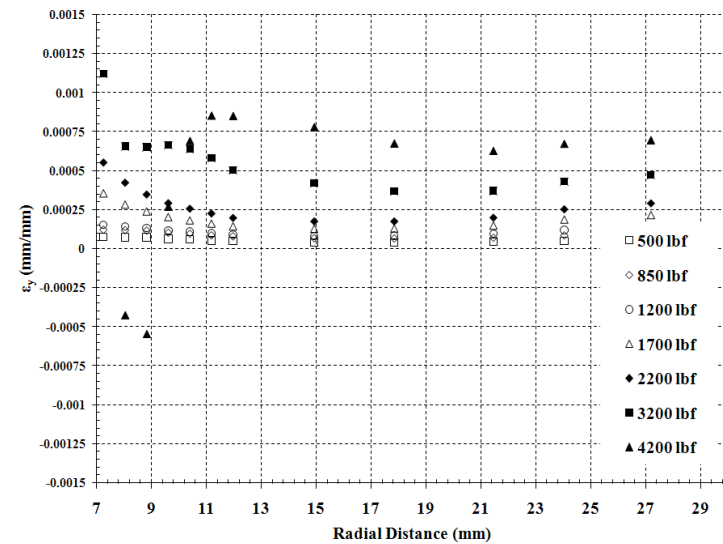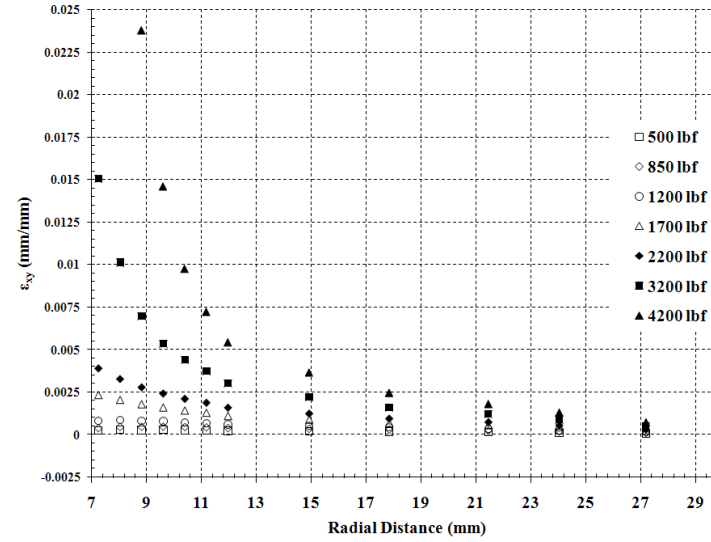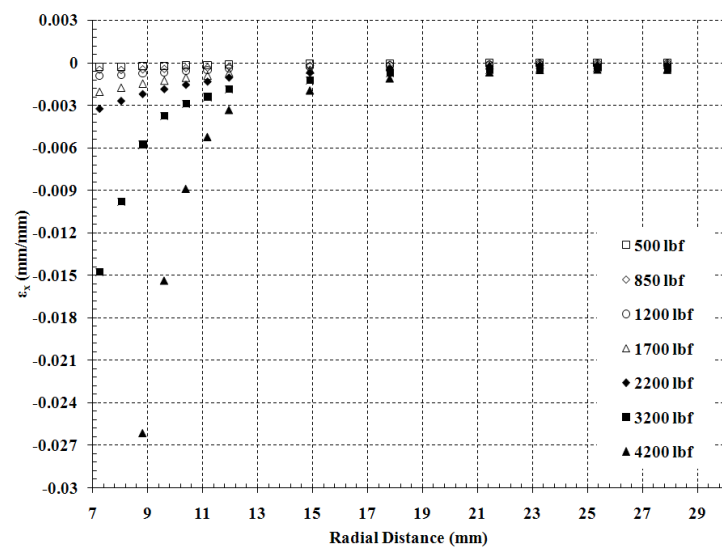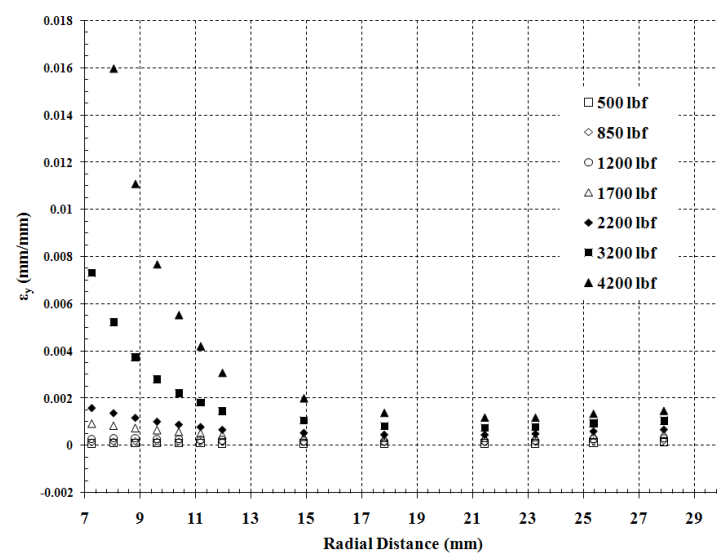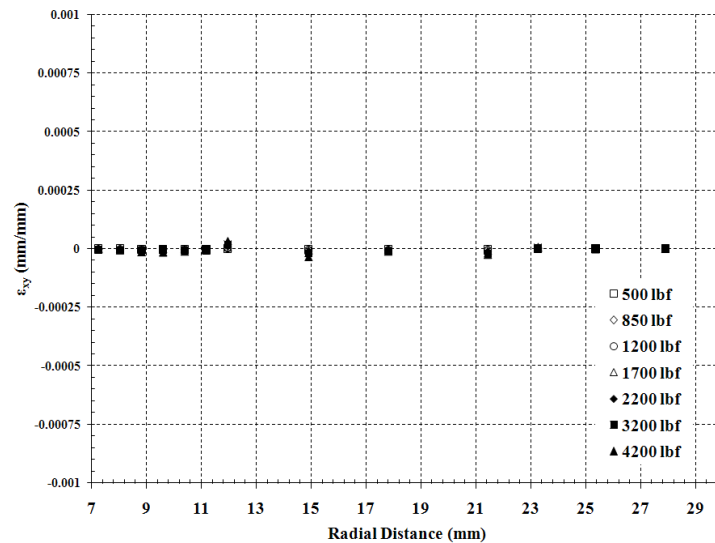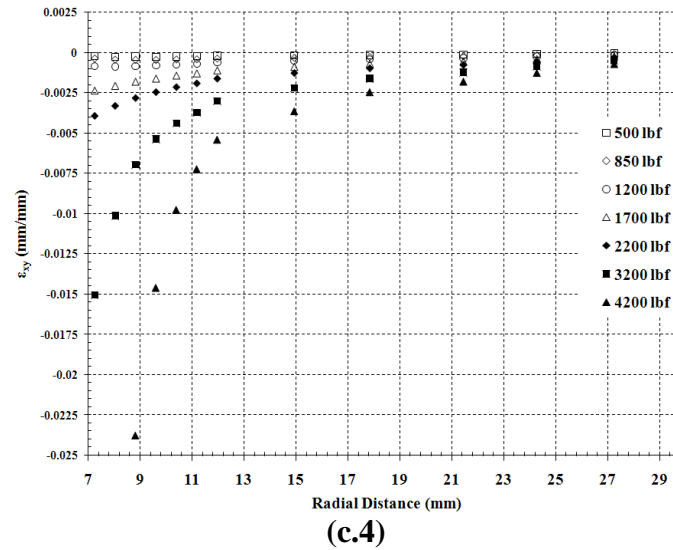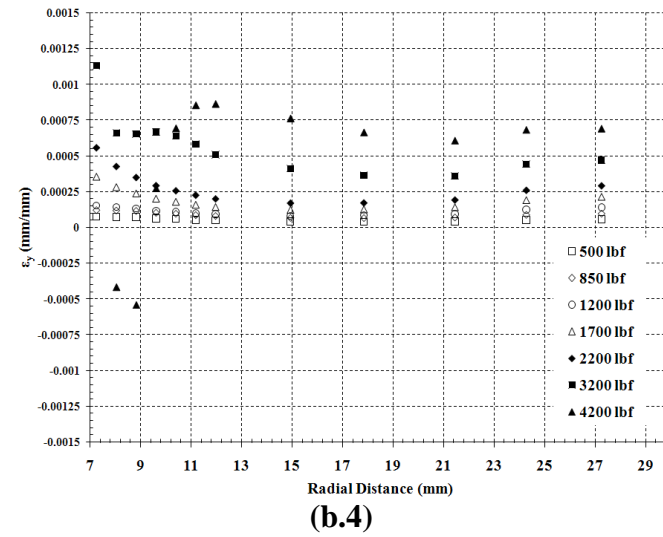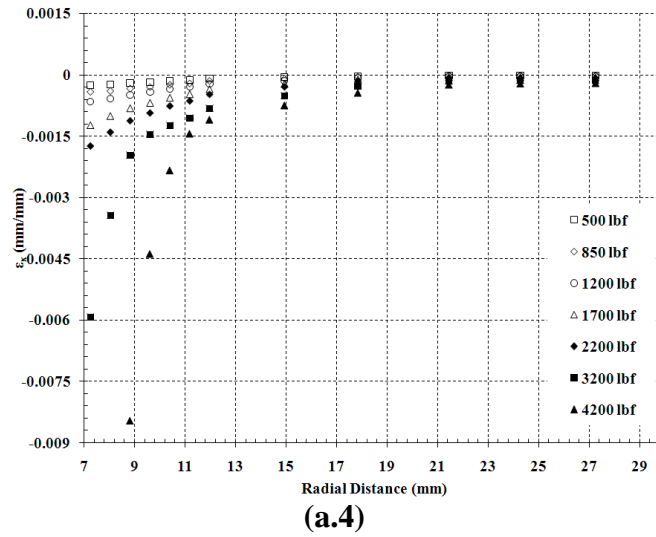
Figure B-1: Model results of the applied load (peak of every cycle) upon the radial variation of in–plane strains (a) ε_x (b) ε_y and (c) ε_{xy} at orientations (1) $\theta = 0°$, (2) $\theta = 153°$, (3) $\theta = 180°$, and (4) $\theta = -153°$ on the self-locking nut side of a joint of specimen
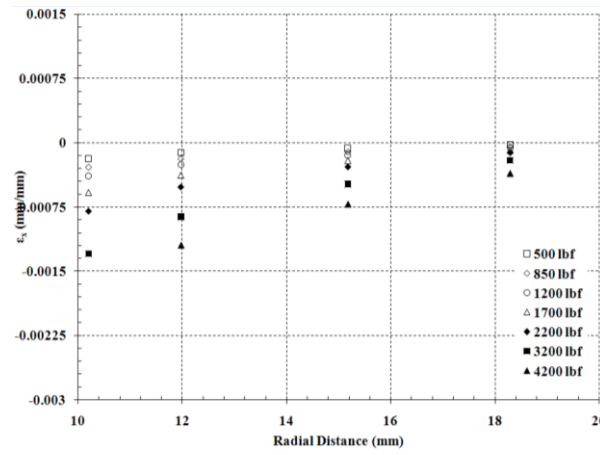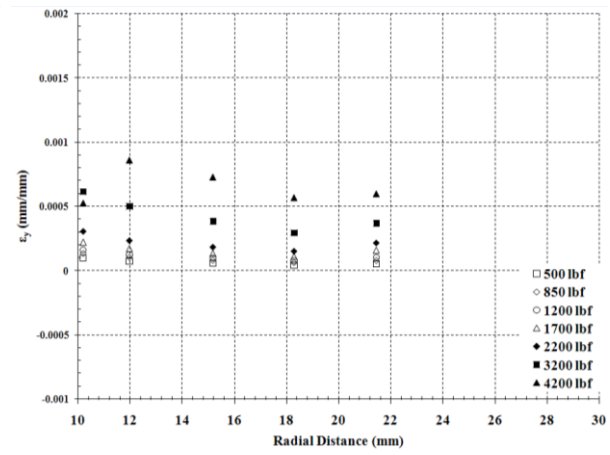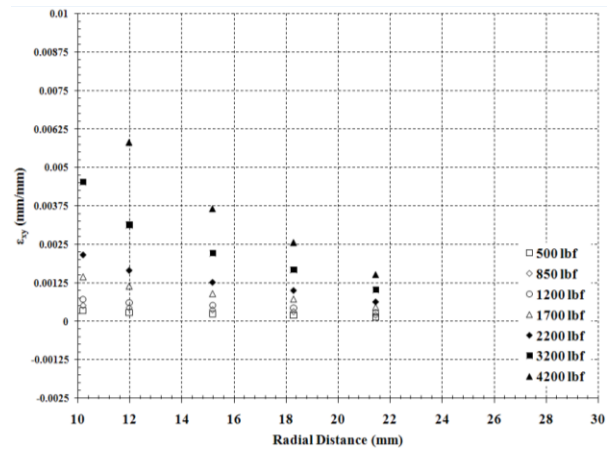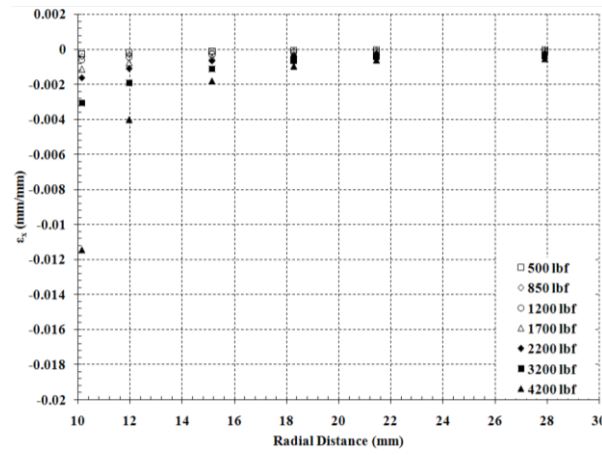
(a.1)

(b.1)

(c.1)

57

(a.2)

(b.2)

(c.2)

(a.3)

(b.3)

(c.3)

59
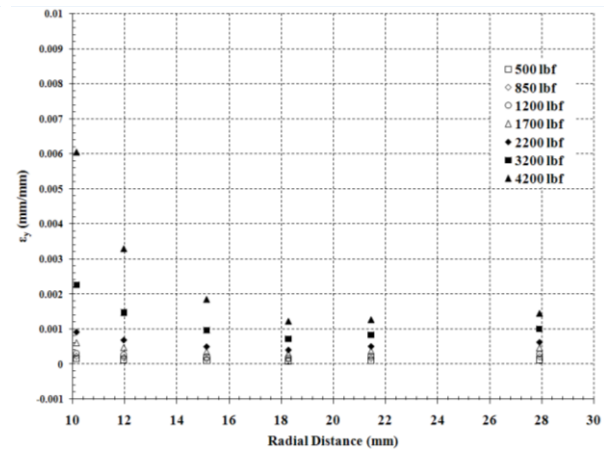
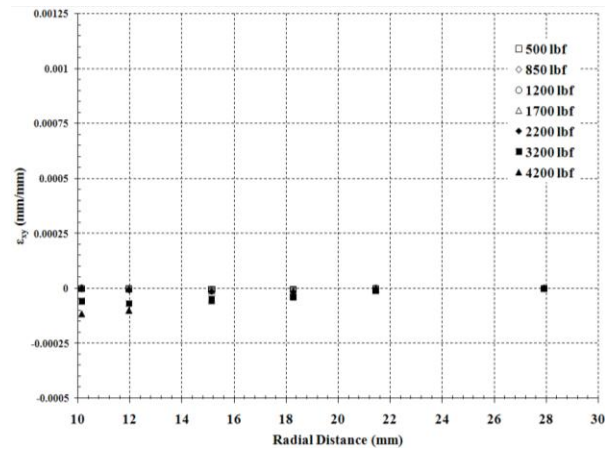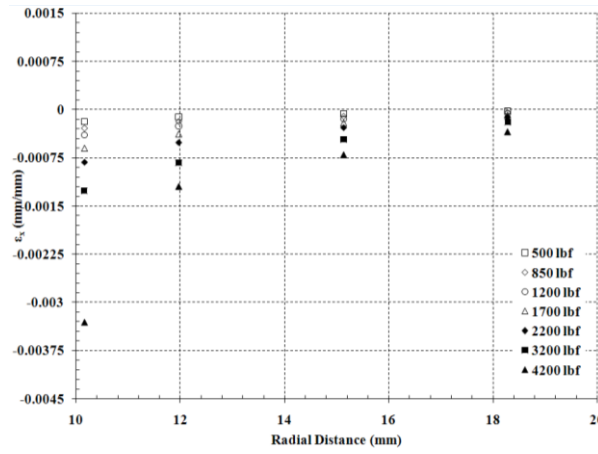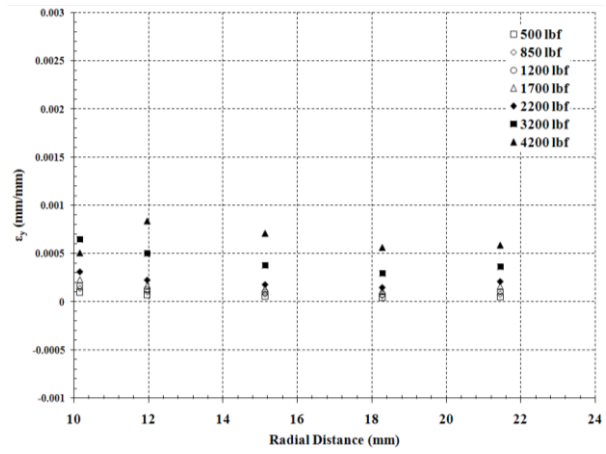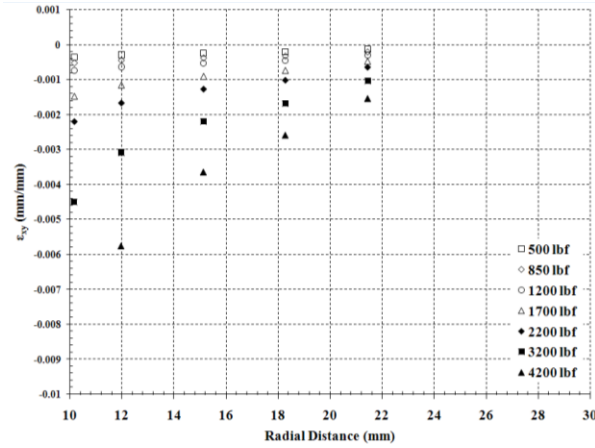**Figure B-2: Model results of the applied load (peak of every cycle) upon the radial variation of in–plane strains (a) ε_x (b) ε_y and (c) ε_{xy} at orientations (1) $\theta = 0°$, (2) $\theta = 153°$, (3) $\theta = 180°$, and (4) $\theta = -153°$ on the bolt head side of a joint of specimen**

60

APPENDIX C – Additional Data

Table C-1: Doubler material model (Al 2024) for ABAQUS/CAE

Doubler Tensile Test Data	
Modulus of Elasticity	9212455 psi
Yield Stress (psi)	Plastic Strain
50421	0
53595	0.00422
56059	0.01004
58210	0.01591
60006	0.02186
61759	0.02781
63415	0.03362
65078	0.03985
66562	0.04571
67931	0.05183
69493	0.05778
70538	0.06394
71756	0.07021
72812	0.07690
74120	0.08298
74901	0.08932
75962	0.09615
76837	0.10357
77972	0.11058
78684	0.11753
79404	0.12391
79891	0.13091

Table C-2: Central plate material model (Al 2024) for ABAQUS/CAE

Central Plate Tensile Test Data	
Modulus of Elasticity	8251196.333 psi
Yield Stress (psi)	Plastic Strain
44072	0
44283	0.00059
44458	0.00121
45585	0.00483
46800	0.00921
47965	0.01360
50071	0.02186
50990	0.02597
51950	0.02996
52794	0.03416
53665	0.03828
54350	0.04223
55102	0.04618
55861	0.05035
56529	0.05457
57193	0.05854
58448	0.06621
58933	0.07038
59529	0.07474
60132	0.07910
60507	0.08327
61124	0.08714
61534	0.09076
62034	0.09441
62318	0.09830
62881	0.10280
63384	0.10795
63931	0.11346
64218	0.11896
64806	0.12407
65179	0.12840
65593	0.13213
65761	0.13542
66094	0.13838
66365	0.14128
66635	0.14433
66772	0.14788
67146	0.15327
67591	0.16281
68165	0.17579
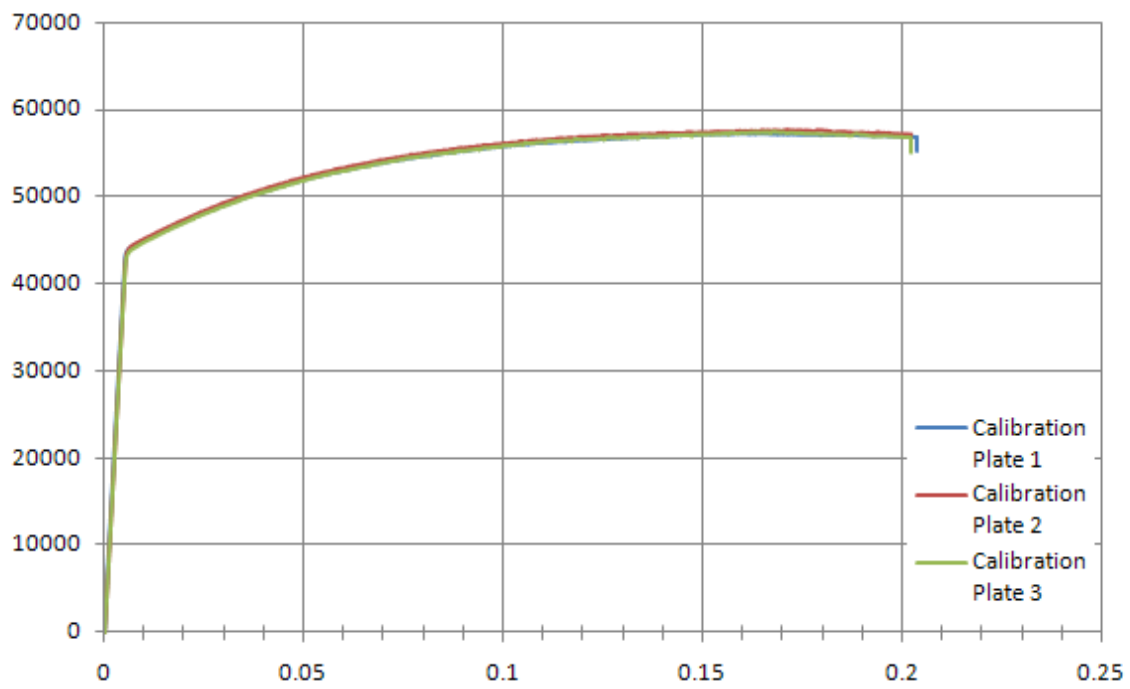
Figure C-1: Calibration plate tensile test results
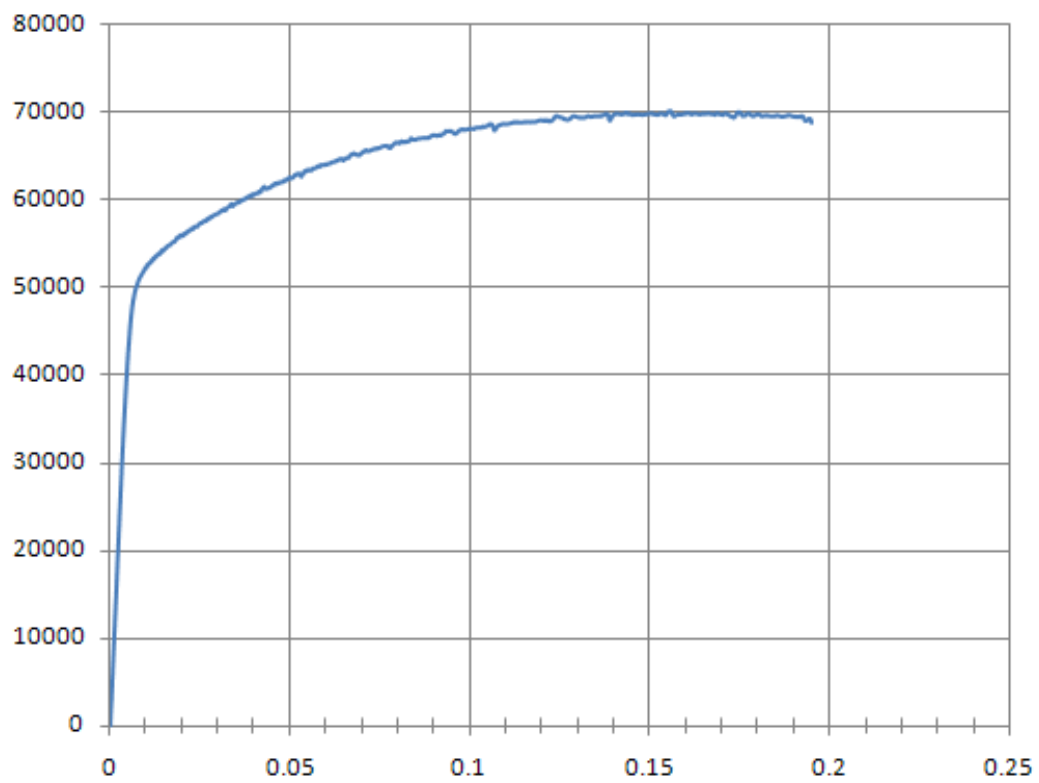
Figure C-2: Doubler tensile test results

LIST OF ACRONYMS, ABBREVIATIONS, AND SYMBOLS

ASTM	American Society for Testing and Materials
DIC	Digital Image Correlation
TSA	Thermoelastic stress analysis
FE	Finite Element
FEM	Finite Element Model
E	Modulus of Elasticity
in-lb	inch-pounds force
fps	frames per second
μ	coefficient of friction
lb	pound force
lb/s	pound force per second
kip	1,000 pounds force
psi	pound force per square inch
ksi	1,000 pounds force per square inch
SAE	Society of Automotive Engineers
σ_y	yield tensile strength
σ_u	ultimate tensile strength
θ	angle from the loading direction axis
ε_x	strain in x-direction
ε_y	strain in y-direction
ε_{xy}	shear strain